Shaking table tests on the stability of dip and anti-dip rock slopes with structural planes induced by seismic motions

Chunlei Xin [a,b], Wenhui Li [a], Zhao Wang [c,*], Wenkai Feng [a,b], Iman Hajirasouliha [d], Xinyuan Yu [d]

[a] State Key Laboratory of Geohazard Prevention and Geoenvironment Protection, Chengdu University of Technology, Chengdu, China
[b] College of Environment and Civil Engineering, Chengdu University of Technology, Chengdu, China
[c] Institute for Transport Studies, University of Leeds, Leeds, UK
[d] Department of Civil and Structural Engineering, The University of Sheffield, Sheffield, UK

A B S T R A C T

Benched rock slopes are prevalent in extensive engineering endeavors such as mining and road construction. This research investigates the dynamic response patterns and failure mechanisms of dip and anti-dip rock slopes through shaking table tests. The adopted approach involves utilizing the acceleration amplification factor (AAF) to compare the amplification effects on both slope types under varying excitation amplitudes. Fourier spectrum analysis of acceleration is conducted to explore the relationship between seismic wave frequency and slope response. The Hilbert-Huang Transform (HHT) method is employed to analyze the differences in seismic response between dip and anti-dip slopes. The results reveal that anti-dip slope exhibits superior stability compared to dip slope, as the latter experiences earlier failure. The study also identifies the critical excitation intensity value ("threshold point"), indicating the evolution of benched slope dynamic response. The findings demonstrate that dip slopes are more significantly affected by seismic motion, exhibiting higher energy concentration and release. The seismic wave propagation in dip slope also shows a greater energy release compared to anti-dip slope. These outcomes should provide valuable insights for the design and seismic disaster risk assessment of benched slope engineering in regions with high seismic activity. The findings highlight the increased risk of slope failure in dip slopes and emphasize the importance of considering slope stability in engineering projects. The approach proposed in this study, along with the identified critical excitation intensity value, can aid in understanding and mitigating the potential risks associated with benched slope engineering.

1. Introduction

Approximately two-thirds of China's land area is covered by mountains, resulting in a widespread presence of natural slopes. Geographically positioned between the circum-Pacific and Eurasian seismic belts, the country also faces compression from the Pacific, Indian, and Philippine Sea Plates, fostering well-developed seismic fault zones with a high frequency of seismic activity (Wen et al., 2021; Xin et al., 2022). Notably, the 2008 Wenchuan Ms8.0 earthquake induced a massive number of landslide disasters, including the Daguangbao landslide, the largest recorded landslide in China and one of the few super large-scale landslides in the world, with over 500 million m³ in volume and creating a landslide dam standing at 690 m, the tallest in the global record (Hu et al., 2021). In 2013, the Lushan County Ms. 7.0 earthquake also triggered landslides and collapses over an area about approximately 1300

km², resulting in about 3000 geological hazards. Likewise, the Jiuzhaigou Ms. 7.0 earthquake on August 8, 2017, triggered around 1900 geological hazards, affecting an area of 8.11 km². As another example, on September 5, 2022, the Luding County Ms. 6.8 earthquake caused 331 collapses and 234 landslides in the heavily affected areas of Luding and Shimian counties. Following this, on December 18, 2023, a magnitude 6.2 thrust earthquake struck in Jishishan County, Linxia Prefecture, Gansu Province, triggering over 1500 geological hazards, primarily comprising of small to medium-scale loess landslides and shallow rock collapses. A noteworthy incident within these events was a special mudflow in Qijiagou, Zhongchuan Township, Minhe County, Qinghai Province, which led to the destruction of 95 houses, disruption of 19 roads, and 13 casualties. The recent surge in earthquake activity has led to a notable rise in landslide disasters, highlighting a strong correlation between the severity of slope instability and failure under

seismic actions, the natural geographical setting, and the influence of human economic development and engineering activities (Hu et al., 2024; Xu et al., 2022). The extensive nature of these engineering activities can diminish the stability of natural slopes, which in turn, directly impacts the safety of the engineering works themselves (Ning et al., 2019; Yang et al., 2023a, 2023b).

The investigation of slope dynamic stability fundamentally relies on understanding the seismic dynamic response of slopes. This response is influenced by internal factors such as topography, lithology, and geological structures (He et al., 2020; Song et al., 2019; Song et al., 2021a, 2021b, 2021c), as well as external factors such as the duration,

amplitude, and frequency of seismic motion (Xu et al., 2023). Currently, large-scale shaking table tests represent the most direct approach for elucidating the dynamic response patterns and failure modes of such systems (Dong et al., 2022; Fan et al., 2016; Xin et al., 2024a). These tests can simulate the complete interaction of seismic waves with slopes, offering a direct observation of their effects. High-precision sensors embedded within slopes enable continuous monitoring of dynamic changes in acceleration, pressure, and displacement (Chen et al., 2020; Zhao et al., 2020).

Researchers have employed shaking table tests to investigate the dynamic response and cumulative damage of slopes caused by
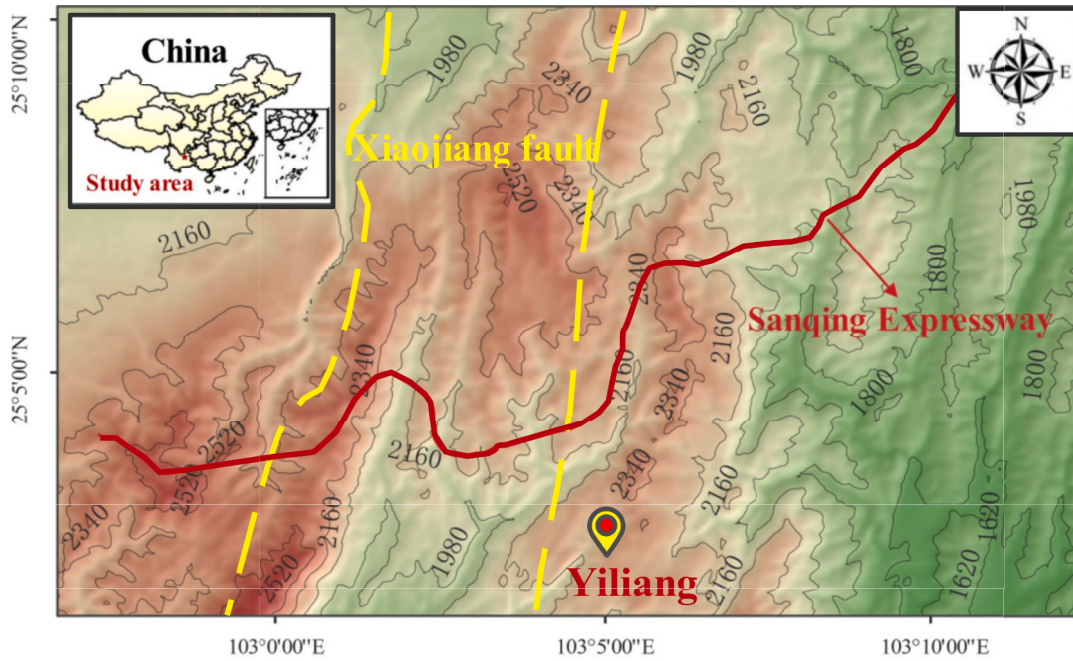
(a)
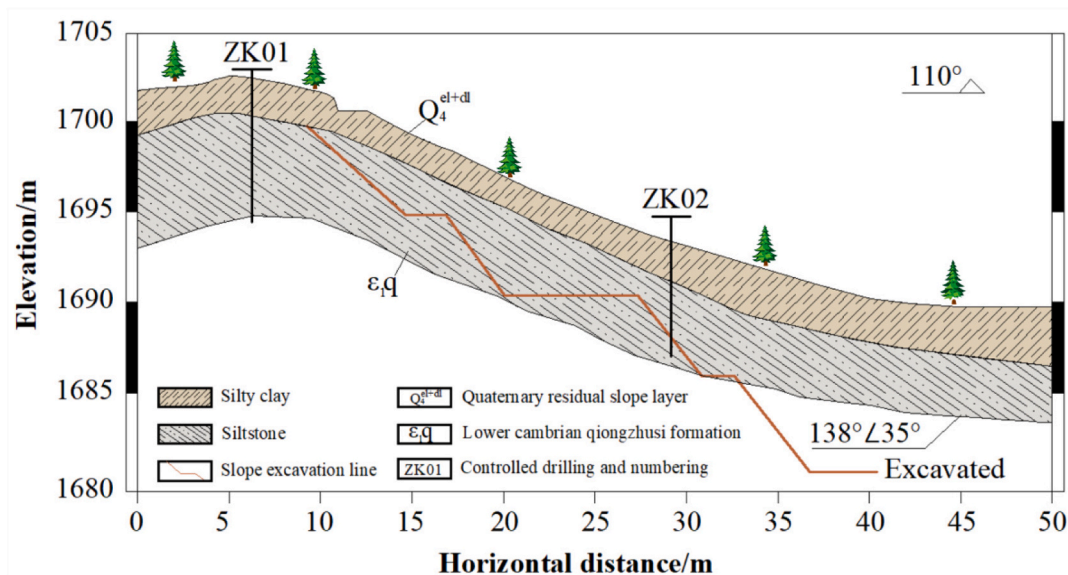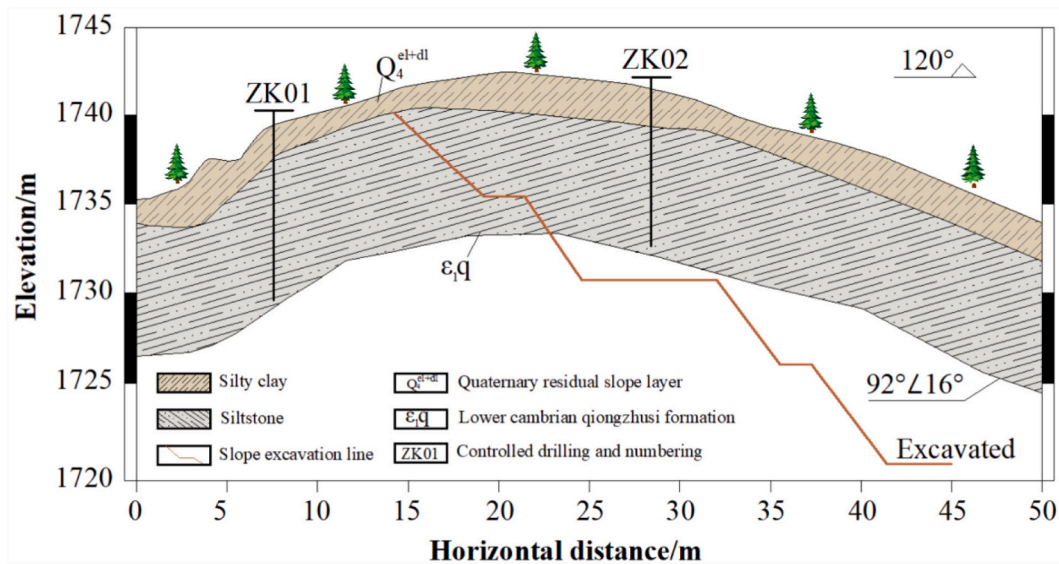

(b)

Fig. 1. On-site investigation and parameter determination of prototype slopes: (a) the location of study area; (b) geological profile of the dip rock slope; (c) geological profile of the anti-dip rock slope; (d) lower portion sampling of the slope between sections K79 + 190 and K79 + 460 and sections K88 + 040 and K88 + 260; (e) instruments of physical and mechanical property test.

(c)

(d)

(e)

Fig. 1. (*continued*).

earthquakes. For instance, a series of shaking table tests were conducted to investigate the influence of a single surface slope on seismic response, revealing the distribution pattern of peak ground acceleration (PGA) under vertical SV wave impact and validating numerical simulation results using a physical model (Qi et al., 2022). Another relevant study examined the dynamic response of bedding rock slopes using three sets of typical joints in large-scale shaking table tests. This study analyzed the effects of input harmonic frequency and joint density on the PGA at the slope surface under vertical SV wave excitation (Tai et al., 2024). Shaking table tests were also employed to explore the cumulative damage to bedding slopes caused by historical earthquakes (Cui et al., 2023). By using the acceleration amplification coefficient and plastic effect coefficient, this study assessed damage accumulation in bedding slopes subjected to multiple seismic events. The findings indicated that the cumulative damage from multiple earthquakes led to a nonlinear amplification of PGA on the slope surface and a nonlinear reduction in the natural frequency of the slope model. Subsequently, a series of shaking table model tests were conducted to examine the time-domain and frequency-domain dynamic responses of slopes to near-fault ground motions. The results indicated that the PGA induced by near-fault ground motions escalated with elevation. However, once the seismic load amplitude exceeded a critical threshold (0.2 g ~ 0.5 g), the intensity of near-fault ground motions increased, leading to reduced PGA amplification with elevation and intensified high-frequency filtering effects of slopes (Bao et al., 2021). To enhance the

understanding of these phenomena, the variation mode decomposition and Hilbert transform method (VMD-HT) were introduced to identify the natural frequencies of slopes. A damage coefficient based on changes in first-order natural frequency of pre- and post-loading conditions was established to study the cumulative damage evolution process of the slope during these tests (Chen et al., 2023). Moreover, several shaking table tests have investigated the effects of rapid water drawdown (RWD) on the seismic response of rock slopes with discontinuities. Through time-frequency analysis, these studies investigated the spectral and energy propagation characteristics of reservoir rock slopes under RWD conditions. The influence of RWD on the slope damage development process was explained through energy-based analytical methods (Song et al., 2021a, 2021b, 2021c). Despite these advances, significant gaps remain in understanding the seismic behavior differences between dip and anti-dip rock slopes, which are crucial for developing effective seismic risk assessment and mitigation strategies.

To address the above research gap, the current study will focus on the dynamic responses of typical dip and anti-dip rock slopes along the Sanbao (Qujing city) to Qingshui (Kunming city) expressway, set against a backdrop of mountainous terrain characterized by frequent seismic activities. To investigate the impact of seismic waves on these slopes, shaking table tests were conducted, utilizing seismic waves with gradually amplitudes recorded at the Wolong station during the Wenchuan earthquake. This approach allowed for a detailed analysis of the dynamic response, covering damage, instability, and failure mechanisms.
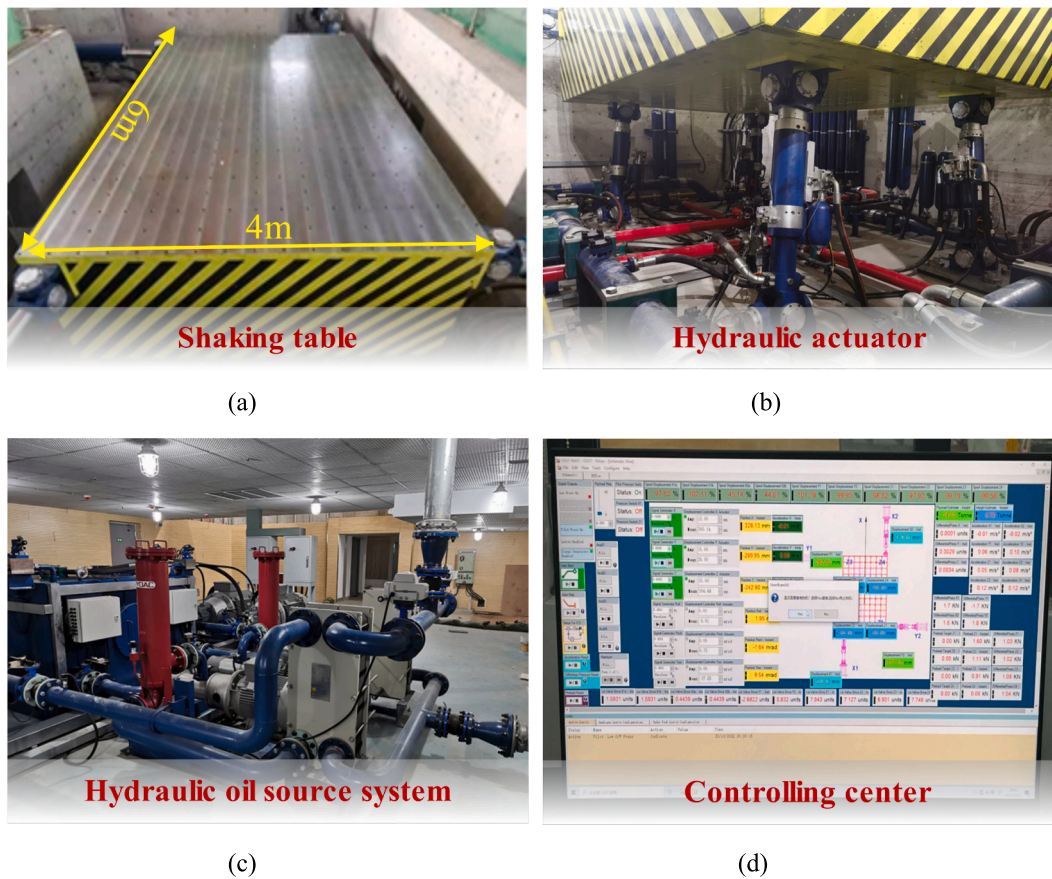
Fig. 2. Shaking table operating systems: (a) shaking table; (b) hydraulic actuator; (c) hydraulic oil source system; (d) computerized control center.

To compare the elevation-dependent variation between dip and anti-dip slopes under different amplitudes of the Wolong wave, a dimensionless factor known as acceleration amplification factor (AAF) was introduced. Furthermore, Fourier spectrum analysis of acceleration was employed to establish the relationship between slope response and seismic wave frequency. The Hilbert-Huang Transform (HHT) method was systematically applied to analyze the differences in seismic response between dip and anti-dip rock slopes, considering failure phenomena, AAF, frequency domain characteristics, and acceleration time-frequency characteristics. By integrating acceleration, Arias intensity, and dynamic characteristics of the model slopes during the excitation process, this study aims to identify critical excitation values that reflect the dynamic response changes of the model slopes. The results obtained enhance our overall comprehension of the dynamic response characteristics displayed by benched rock slopes under seismic conditions, thereby offering valuable insights for the formulation of strategies related to disaster risk assessment and mitigation for slope engineering.

2. Geological setting of the study slope

This study focuses on the ongoing construction of the Sanqing Expressway, specifically the segment connecting Sanbao (Qujing city) to Qingshui (Kunming city), situated within the high seismic intensity zone. Understanding the seismic response and developing effective disaster mitigation strategies of the slope are crucial for this expressway and similar infrastructure projects in the high seismic intensity zone of Southwest China. Two representative rock slope sections along the Sanqing Expressway were chosen for detailed investigation. Fig. 1(a) respectively depict the geographical location map and contour map of the study area. The first selected slope is located between sections K79 + 190 and K79 + 460 of the Sanqing Expressway. Borehole sampling,

predominantly showing cake-like or short columnar shapes, revealed that this section primarily comprises highly weathered siltstone with low cementation. The stratum occurrence corresponds to approximately 138°∠35°, and the relationship between the rock stratum and the slope aspect indicates a dip slope configuration as shown in Fig. 1(b). The second selected slope is located between sections K88 + 040 and K88 + 260 of the Sanqing Expressway. In this research area, approximately 40 % of the land is covered by vegetation, which includes both trees and cultivated lands. Borehole sampling from this slope revealed that the overlying strata in the roadbed area consist of Quaternary Holocene residual slope deposits (Q_4^{dl+el}), comprising reddish-brown clay with a hard-plastic consistency and approximately 5 % ginger stone particles ranging in size from 2 to 20 mm. The predominant lithology in this section is highly weathered siltstone. The stratum occurrence corresponds to approximately 92°∠16°, and the relationship between the rock stratum and the slope aspect indicates an anti-dip slope configuration as shown in Fig. 1(c). Field sampling was also conducted on the selected slopes (as shown in Figs. 1(d)), followed by laboratory direct shear tests and uniaxial compression tests (Fig. 1(e)). The direct shear tests involved the preparation of standard specimens, which were then subjected to incremental shear tests under normal stresses of 0.5 MPa, 1.0 MPa, 1.5 MPa, and 2.0 MPa. Uniaxial compression tests were conducted on cylindrical specimens, each with a diameter of 50 mm and a height of 100 mm, compressed until failure.

3. Shaking table model test

3.1. Test device

The shaking table test system utilized in this study was provided by the Seismic Simulation Shaking Table Laboratory, belonging to the State

Table 1
The similarity relationship and similarity ratios.

Number	Parameter	Similarity relation	Similarity ratio
1	Geometric dimension (L)	Dominating variable	$C_L = 25$
2	Acceleration (a)	Dominating variable	$C_a = 1$
3	Density (ρ)	Dominating variable	$C_\rho = 1$
4	Elastic modulus (E)	$C_E = C_L C_\rho C_a$	$C_E = 25$
5	Poisson's ratio (μ)	–	$C_\mu = 1$
6	Cohesion force (c)	$C_c = C_L C_\rho C_a$	$C_c = 25$
7	Internal friction angle (φ)	1	$C_\varphi = 1$
8	Stress (σ)	$C_\sigma = C_L C_\rho C_a$	$C_\sigma = 25$
9	Strain (ε)	1	$C_\varepsilon = 1$
10	Time (t)	$C_t = C_L^{1/2} C_a^{-1/2}$	$C_t = 5$
11	Displacement (d)	$C_d = C_L$	$C_d = 25$
12	Velocity (v)	$C_v = C_L^{1/2} C_a^{1/2}$	$C_v = 5$
13	Damping ratio (ζ)	–	$C_\zeta = 1$

Table 2
The physical mechanical parameters of rock mass.

Rock mass	Density ρ (kg/m^3)	Elastic modulus E (Mpa)	Cohesion c (kPa)	Internal friction angle φ (°)	Poisson's ratio (μ)
Prototype	2250	780	493	36	0.32
Model	2200	50	20	36	0.34

Table 3
The physical mechanical parameters of structure plane.

Structure plane	Cohesion c (kPa)	Internal friction angle φ (°)	Normal stiffness k_n (Gpa/m)	Shear stiffness k_s (Gpa/m)
Prototype	493	36	3.9	2.5
Model	20	36	3.5	2.3

Key Laboratory of Geohazard Prevention and Geoenvironment Protection at Chengdu University of Technology (see Fig. 2). The shaking table equipment was manufactured by SERVOTEST company, a renowned company based in the United Kingdom. The system features a table measuring 4 m × 6 m (width×length), equipped with four vertical actuators, four horizontal actuators, a hydraulic power source with a capacity of 1500 l @ 28Mpa, a hydraulic power control system, and a Pulsar vibration input control system. The maximum load capacity of the shaking table is 4.0×10^4 kg, while the actuators can produce maximum load accelerations of 1.5 g horizontally and 1.0 g vertically,

with maximum displacements of 300 mm and 150 mm, respectively. It is worth mentioning that, in general, shaking table systems may experience waveform distortion due to insufficient stiffness of the connecting components, high harmonic vibrations resulting from local vibrations of the table, and the interactive effect of the specimen and the table. Therefore, to verify the accuracy of the test data in this study, both displacement and acceleration distortions of the shaking table were thoroughly examined. The results indicated that the three-axis displacement distortion (X, Y, and Z) of the shaking table was less than 3 %, and the three-axis acceleration distortion met the requirement of being under 5 %. Therefore, it was concluded that the waveform generated by the shaking table satisfies the specified accuracy criteria.

3.2. Scaled model

To maintain similarity between the model and the prototype, the shaking table test must adhere to the similarity relationship in both static and dynamic conditions. In this study, acceleration (g), density (ρ), and geometric dimension (L) were chosen as the primary control variables (Xin et al., 2018). Based on the Buckingham π theorem, the geometric similarity ratio (C_L) between the prototype and the model was established at $C_L = 25$. This ratio guided the construction of the slope model to dimensions of 2 m in length, 0.7 m in width, and 1 m in height. The similarity relationship and dimensional representation of shaking table tests are shown in Table 1.

In order to obtain precise physical and mechanical parameters for the slope model, a range of laboratory tests, including direct shear tests, uniaxial compression tests, and standard triaxial tests, were performed. These tests provided the strength parameters and mechanical characteristics of the rock mass and its structural planes as outlined in Table 2 and Table 3. The target values for various physical and mechanical parameters of the model material were determined based on the established similarity relationship. Orthogonal experimental results of the similarity material ratio for the slope model were also used to select the optimal ratio of barite powder, bentonite, gypsum, paraffin oil, and water in a mass ratio of 65:13:5:13:3, as shown in Fig. 3. Barite powder served as fine aggregates, while gypsum and water acted as binders, and paraffin oil functioned as a water-retaining agent. Considering the significant influence of structural planes on the deformation, strength, and stability of the rock slope, precise simulation of these features is essential for obtaining reliable test outcomes.

In this study, the film units measuring 15 cm × 10 cm were utilized to simulate structural planes within the inclined-layer slope model, and the mechanical parameters of the structural planes were determined through direct shear tests. The connectivity rate of structural planes
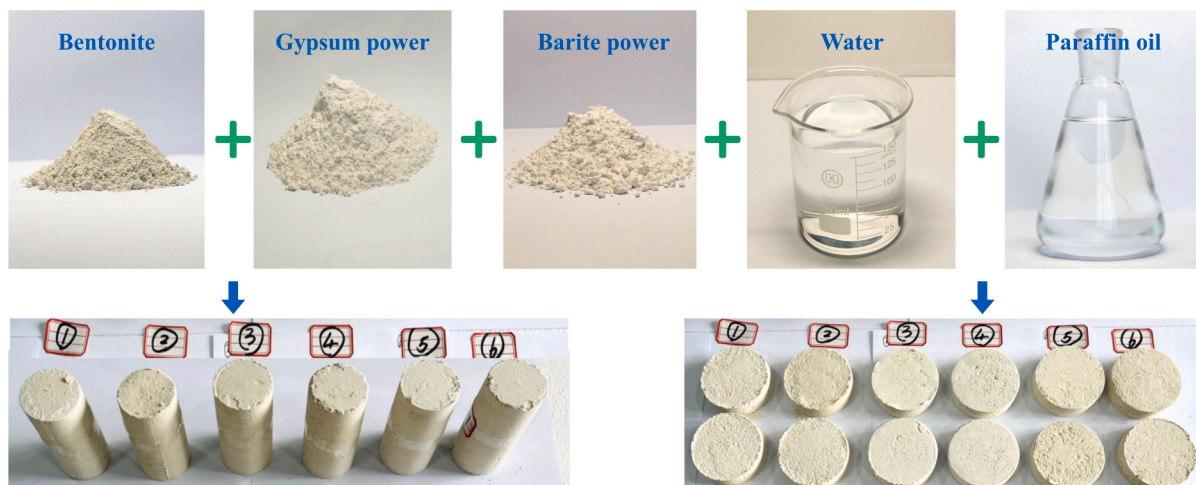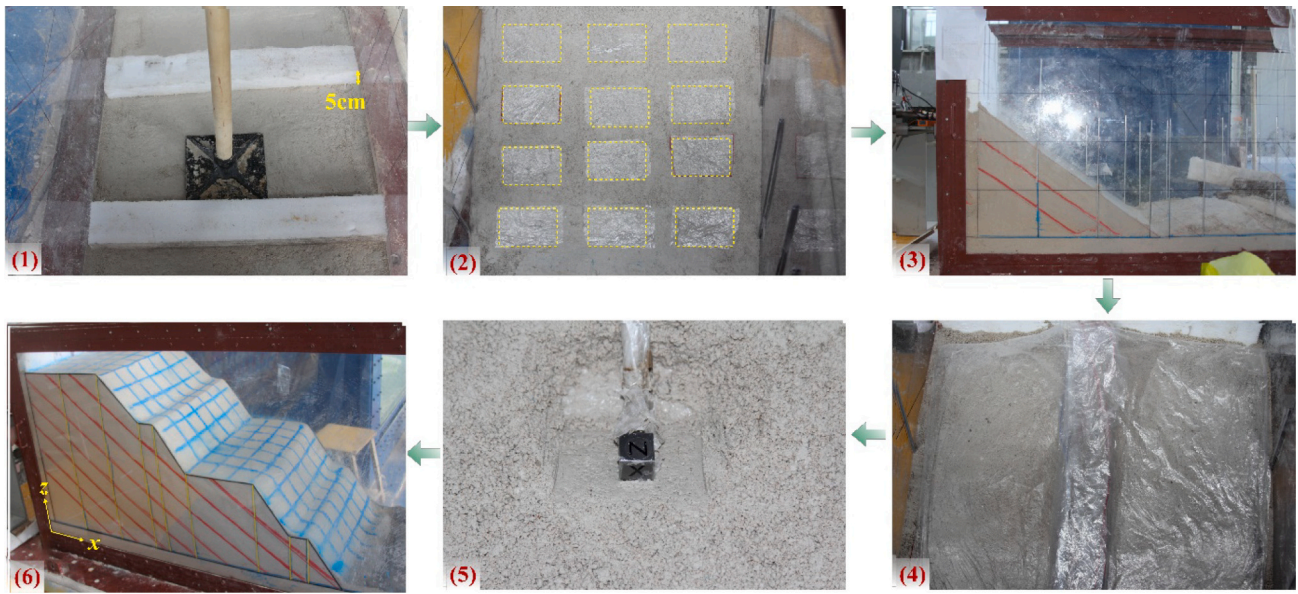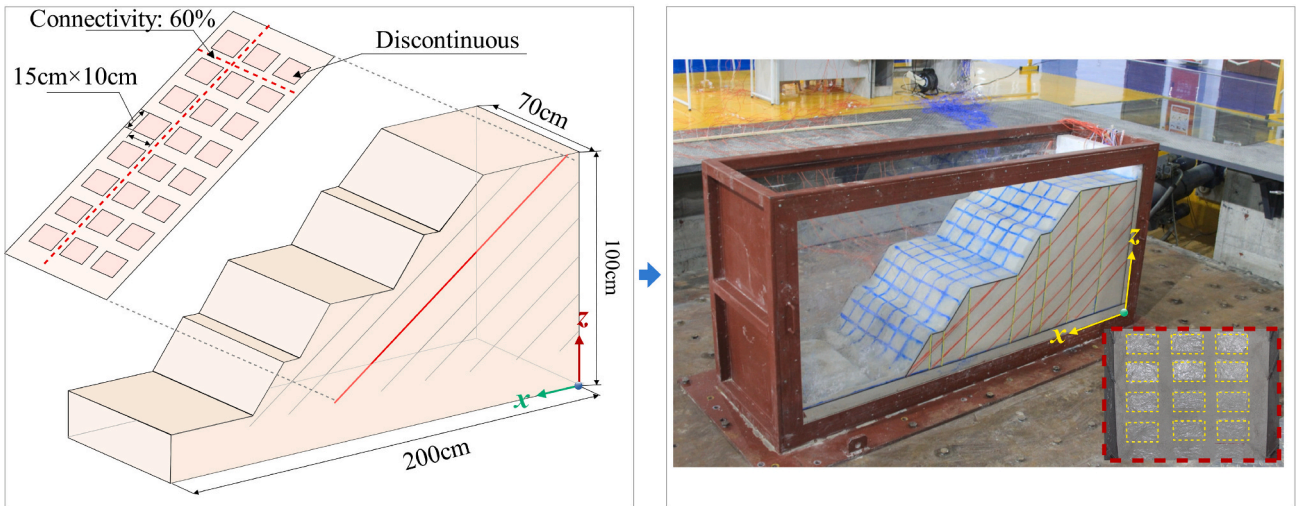

Fig. 3. Similar materials and specimens of the model slope.

(a)

(b)

Fig. 4. Construction process and testing scheme of the slope model: (a) construction process of the slope model; (b) testing scheme of the slope model.

refers to the proportion of connected structural planes within a certain area in the interconnected network system formed by the structural planes. The connectivity rate for these structural planes was determined based on the field observations of vertical spacing, the internal friction angle of the rocks, and the average length of individual structural planes, as indicated by Eqs. (1) and (2).

$$k_l = \frac{L_{cp}}{L_{cp} + L_k} \tag{1}$$

where, k_l represents the connectivity rate, L_{cp} represents the average length of a single structural plane, and L_k denotes the modified value derived from the average spacing of the structural planes in accordance with the rock failure criterion, calculated using the following equation:

$$L_k = \frac{a}{sin\left(45° - \frac{\varphi}{2}\right)} \tag{2}$$

where, φ represents the internal friction angle of the rocks, and a denotes the vertical spacing of the structural planes.

A connectivity rate of 60 % was assigned to the structural planes in the shaking model tests, aligning with similar approaches adopted by other researchers (Cui et al., 2024; Yang et al., 2023a, 2023b).

The prototype slope was designed as a three-level platform benched slope, where each bench was 5 m in height. The first and third benches were 2 m wide, while the second bench had a width of 8 m. Reflecting to the geometric similarity ratio of 1:25, each bench in the model slope measured 20 cm in height, with the widths of the first and third benches set at 8 cm and the second bench at 32 cm. In the prototype area of the
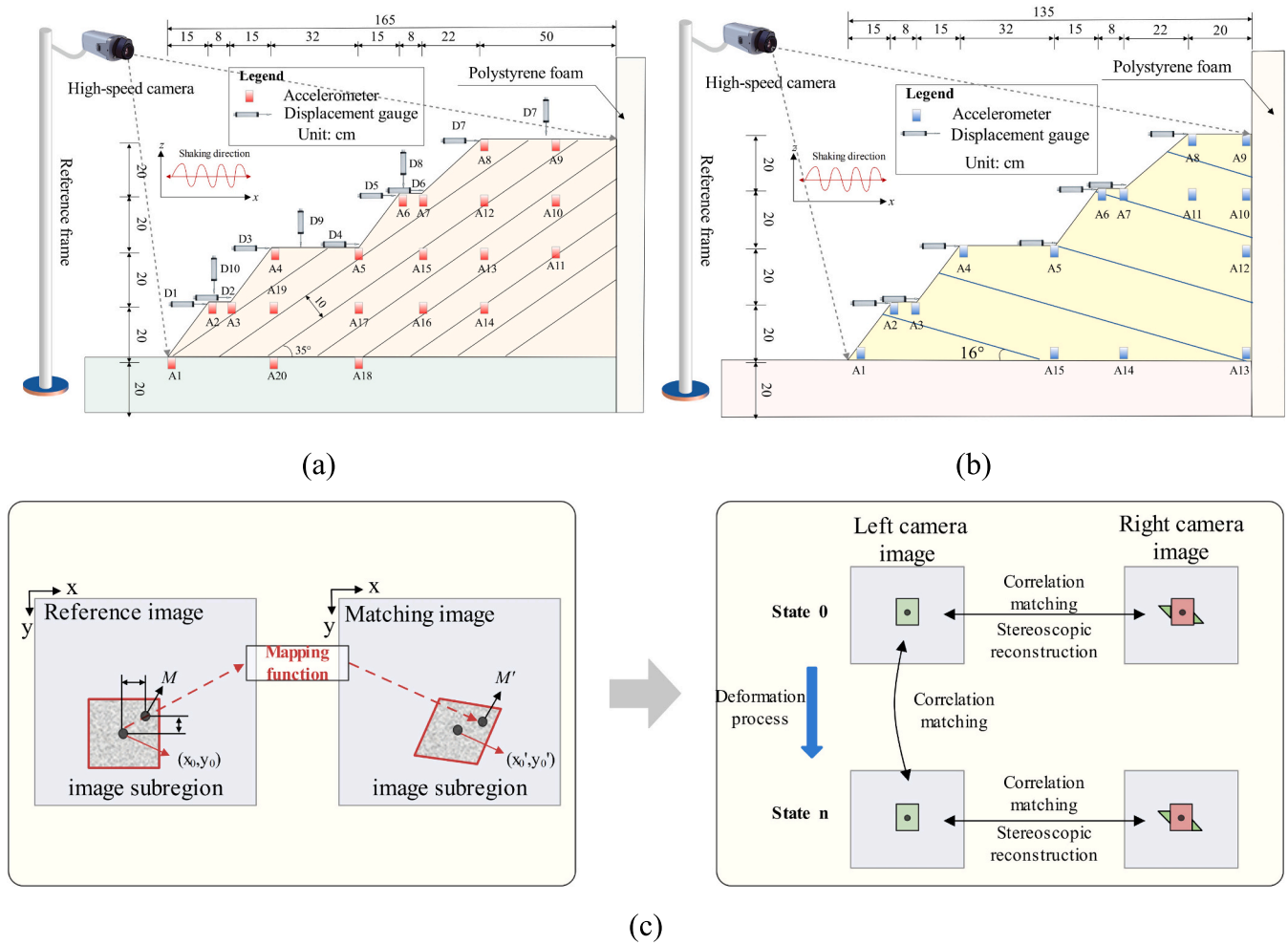
Fig. 5. Monitoring schemes and site arrangement for shake table tests: (a) monitoring scheme of dip slope; (b) monitoring scheme of anti-dip slope; (c) the underlying principles of XTDIC.

Table 4
Ground motion parameters of Wolong (WCW) station.

Monitoring stations	Components	Fundamental frequency/Hz	Focal depth/km	PGA cm/s²
051WCW	EW	2.4		957.700
051WCW	UD	8.1	14	948.103
051WCW	NS	6.9		652.851

slope, the average length of a single structural plane is 20 cm, and the vertical spacing between structural planes ranges from 5 to 8 cm. In the paper, a vertical spacing of 7 cm for the structural planes is assumed. The internal friction angle of the rock is 36°. In the dip slope model, the structural planes exhibited an inclination angle of 35°, while in the anti-dip slope model, the structural planes featured an inclination angle of 16°. Fig. 4 illustrates the construction process of the benched rock slope, which begins with marking the slope outline and the positions of the structural planes on the organic glass before filling the model. The materials of the slope were mixed uniformly according to the designated proportions. Subsequently, the filling of the slope proceeded in layers, from the base upwards, with meticulous attention to controlling the thickness of each layer at approximately 5 cm. The material was then compacted using a tamping hammer to achieve the desired density, ensuring compliance with the similarity relationship. Thin film units measuring 15 cm × 10 cm, were utilized to simulate the structural planes, with a 60 % connectivity rate implemented in each layer. To

protect the model against external environmental effects and ensure the integrity of test results, each construction phase was followed by covering the model surface with a protective film. This measure served to maintain the reliability of the test results and guarantee the accuracy (Xin et al., 2019). Sensor installation was carefully managed during the layering process. Accelerometers, earth pressure cells, and displacement gauges for the test were strategically placed within the model, while sensors were waterproofed by wrapping them in tape, enhancing their operational reliability. Upon completion of the model, to enable accurate monitoring of slope displacement under seismic actions, a grid with 10 cm spacing was drawn on the bench slope surface, and reflective markers were placed at grid intersections.

3.3. Measuring Systems

The monitoring scheme employed during the shaking table test is presented in Fig. 5. Various instruments, including accelerometers, earth pressure cells, displacement sensors, extended three-dimensional digital image correlation (XTDIC) system, and cameras, were utilized to record and monitor the failure mechanism in the slope under seismic wave loading. Accelerometers and earth pressure cells were embedded at the internal corner and external corner of the bench as well as inside the slope body. Displacement gauges were placed on the slope surface. Specifically, IEPE piezoelectric accelerometers were selected, with a type of 1A314E, a measurement range of ±50 g, a frequency response range of 0.5–700 Hz for the X/Y/Z axes, and an axial sensitivity of 10.10
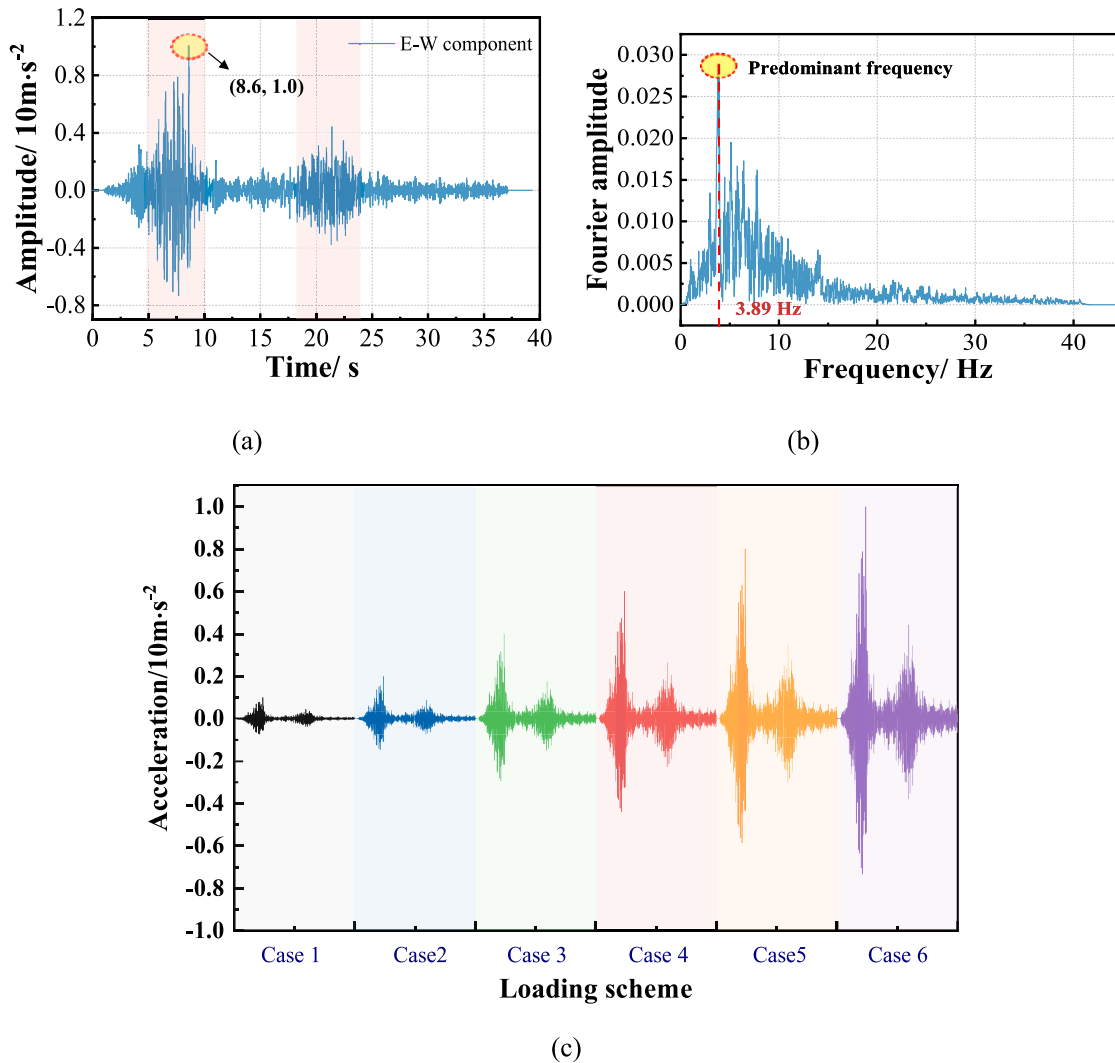
(a)

(b)

(c)

Fig. 6. Input ground motion and loading scheme for shaking table test: (a) the time history of Wolong seismic wave; (b) the Fourier spectrum of Wolong seismic wave; (c) loading scheme.

mV/ms^2 for the X-axis. The earth pressure cells with a type of BW were employed, offering a measurement range of 1 MPa, a sensitivity of 5 mV/MPa, and a diameter of 28 mm. The displacement gauges utilized were MIRAN KTR11 rebound-type displacement gauges, capable of measuring within a range of 100 mm with an accuracy of 0.01 mm. The XTDIC three-dimensional full-field strain measurement and analysis system were combined with binocular vision microscope technology to measure the three-dimensional coordinates and displacement fields on the surface of the slope model during deformation. Digital Image Correlation (DIC) technique was utilized to track the deformation process of speckle patterns on the object's surface. By calculating changes in the grayscale values of the speckle field, DIC provided valuable information regarding the measured surface deformation (as depicted in Fig. 5(c)).

3.4. Input Motion

The seismic loading input for the shaking table test was chosen as the ground motion recorded at the Wolong Station during the 2008 Wenchuan earthquake. The recorded seismic waves at the Wolong Station encompassed components in the east-west (EW), up-down (UD), and north-south (NS) directions, with peak accelerations of 957.7 cm/s^2, 948.1 cm/s^2, and 652.9 cm/s^2, respectively (as detailed in Table 4). Among these components, the EW component from the Wolong Station recordings was selected as the loading input for the shaking table test.

The excitation loading direction on the shaking table was aligned with the horizontal X-axis, which indicates the input seismic wave in the X-direction represented a horizontal shear wave. The duration of the seismic wave excitation is 36 s, as depicted in Fig. 6(a). Spectrum analysis revealed that the energy of the seismic wave was primarily concentrated within the time domain of the first 5–10 s and 17–23 s, with the frequency domain being centered around 3–7 Hz, as shown in Fig. 6(b). To evaluate the failure process and failure modes of the slope model under different excitation amplitudes, six loading cases were defined: 0.1 g, 0.2 g, 0.4 g, 0.6 g, 0.8 g, and 1.0 g. These scenarios aimed to investigate the variations in slope dynamic response and damage mechanisms under seismic actions with increasing intensity levels, as well as to compare the failure modes of dip slope and anti-dip slope subjected to seismic forces (Xin et al., 2020). Before initiating each excitation, a Gaussian white noise with an amplitude of 0.05 g was applied to obtain the natural frequencies of the model slope. The loading scheme for the tests is presented in Fig. 6(c).

4. Analysis of the test results

4.1. Acceleration amplification factor analysis

The original acceleration dataset was processed in MATLAB software for baseline correction and bandpass filtering (0.1–60 Hz). For the
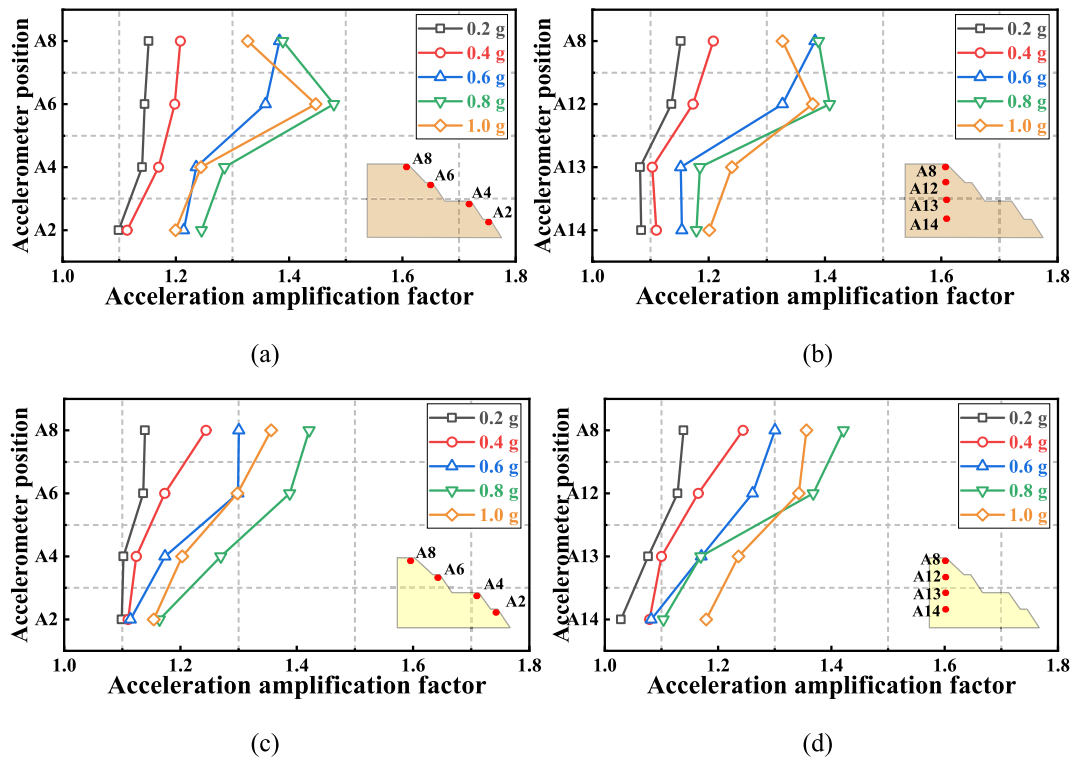
Fig. 7. Acceleration amplification factors of dip slope and anti-dip slope models: (a) AAFs of dip slope model for the slope surface; (b) AAFs of dip slope model for the inside of slope body; (c) AAFs of anti-dip slope model for the slope surface; (d) AAFs of anti-dip slope model for the inside of slope body.

acceleration time history curves, the absolute maximum value was identified as the peak value, which reflects the maximum seismic inertia force within the slope (Yang et al., 2018). The peak horizontal acceleration represented the maximum acceleration in the horizontal direction. To provide a better representation of the slope's response relative to the input wave during seismic action, the concept of dimensionless acceleration amplification factor (AAF) is adopted. The AAF is defined as the ratio of the peak response acceleration at any point within the slope to the peak response acceleration on the shaking table.

Fig. 7 illustrates the AAF variation along the elevation for both dip slope and anti-dip slope models subjected to different excitation amplitudes. It reveals an increase in the AAF along the slope and at slope surface with relative elevation, indicating a pronounced elevation amplification effect (EAE). The stress state within the interior of the slope remains relatively stable in comparison to the slope surface, demonstrating higher resistance to seismic disturbances. The analysis of AAF values for both the interior and surface of the slopes, as shown in Fig. 7, indicates that the AAF at the slope surface surpasses those within the slope interior. This observation highlights the presence of a surface amplification effect (SAE) in such cases. Moreover, the AAF trends nonlinearly upwards with increasing excitation amplitude, becoming especially noticeable at a 0.4 g threshold. This nonlinear behavior can be attributed to the emergence of cracks in the slope under 0.4 g loading, with each crack acting as a propagation interface for the seismic wave. As seismic waves propagate through these cracks, they undergo complex refraction and reflection, also affected by the uneven distribution of seismic wave energy across time and frequency domains. This results in a nonlinear acceleration response of the slope. Comparing the AAF between dip slope and anti-dip slope under excitation amplitudes from 0.1 g to 0.6 g, it is evident that the AAF of the dip slope generally exceeds that of the anti-dip slope. However, as the excitation amplitude increases, the dip slope exhibits earlier failure compared to the anti-dip slope. When the excitation acceleration amplitude reached 1.0 g, severe damage occurred at the slope shoulder (A8) of the dip slope, with numerous rock blocks falling to the second bench under the action of

high-amplitude seismic waves. Tensile cracks appeared at the crest of the slope, in the process of instantaneous dynamic extension, tensile cracks on the slope rapidly propagated, further increasing the slope failure. The occurrence of numerous cracks in the slope fragmented it into loose blocks, reducing the integrity of the slope and lowering its inherent frequency. This leads to an enhanced filtering effect and increased isolation and damping effects on the slope. At this point, the acceleration amplification effect at the dip slope shoulder position (A8) is weaker than that at the anti-dip slope.

4.2. Fourier spectrum analysis

In the series of shaking table tests, white noise scans were conducted on both the dip slope and anti-dip slope models before seismic loading. The transfer functions of each slope model were plotted using Matlab. The frequencies corresponding to the peak points of the transfer function curves can be approximately considered as the natural frequencies of the slopes. From Fig. 8(a) and Fig. 8(b), it can be observed that the natural frequency of the dip slope is approximately 22 Hz, while the natural frequency of the anti-dip slope is approximately 25 Hz.

The Fourier spectrum analysis of the acceleration is conducted to provide a close relationship between the slope's response and the frequency of seismic waves. The results indicate that as seismic waves propagate upward through the slope, selective amplification of certain frequency ranges occurs, while other frequency ranges weaken correspondingly (Che et al., 2016). Comparing the Fourier spectra of the input seismic wave acceleration with the acceleration Fourier spectra at the monitoring points (A8 and A14) for both the dip slope and the anti-dip slope under a 0.6 g excitation amplitude, it is evident that the slope amplifies specific frequency components of the seismic waves, resulting in the observed acceleration amplification. The Fourier spectrum analysis of the horizontal acceleration component also reveals that the amplification of acceleration with elevation is attributed to the slope amplifying a particular frequency component of the seismic wave. Sections of the slope with a relative elevation h/H ≥ 0.5 are most
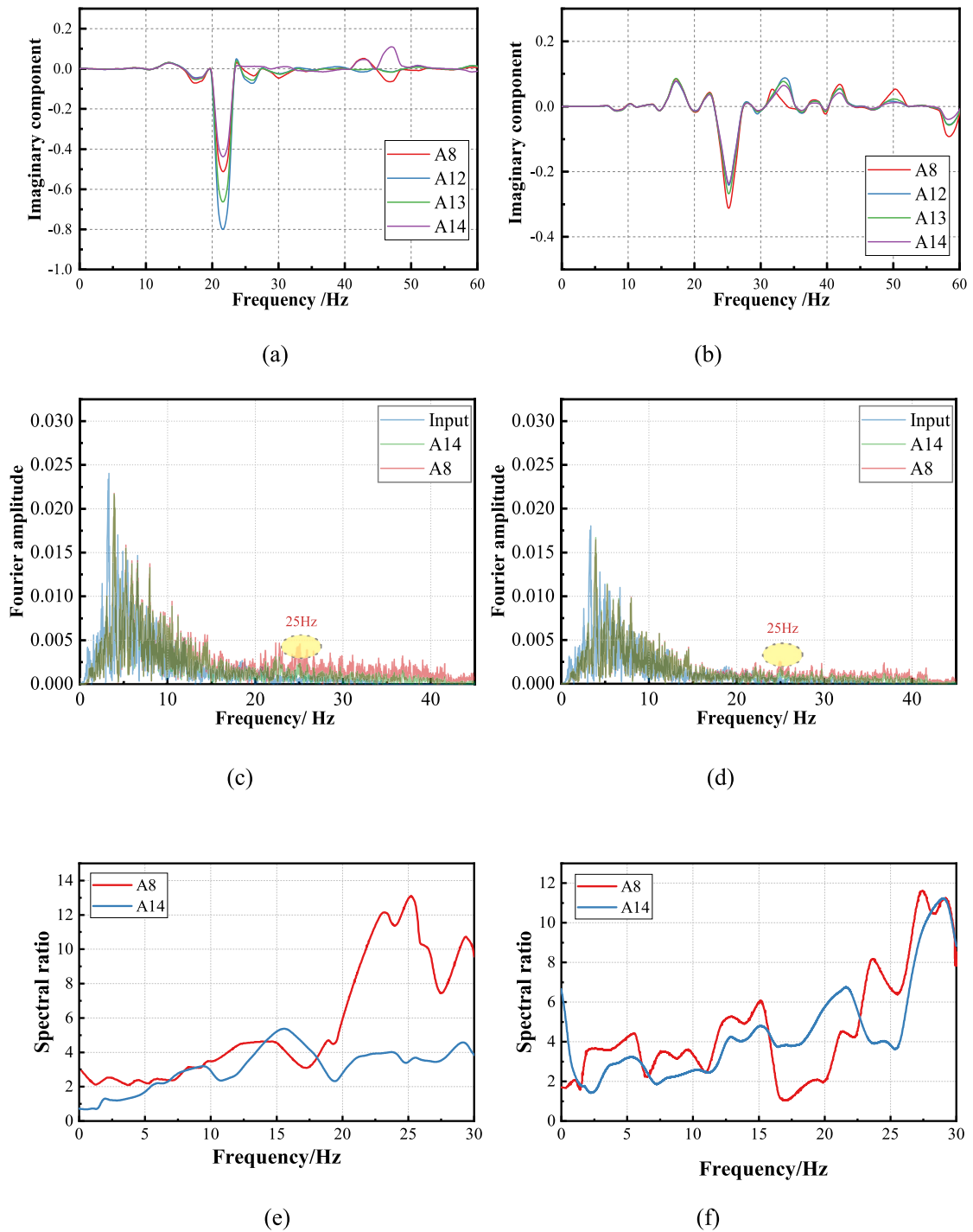
Fig. 8. Transfer functions and Fourier analysis of the dip slope and anti-dip slope: (a) transfer function curve of dip slope; (b) transfer function curve of anti-dip slope; (c) Fourier spectrum of acceleration of dip slope at 0.6 g; (d) Fourier spectrum of acceleration of anti-dip slope at 0.6 g. (e) the spectral ratio of dip slope when the input peak acceleration was 0.6 g; (f) the spectral ratio of anti-dip slope when the input peak acceleration was 0.6 g.

susceptible to frequency amplification changes, making the nonlinear variation of the AAF more pronounced at higher elevation levels. This observation is consistent with the nonlinear AAF model depicted in Fig. 7, underscoring the complex interaction between seismic wave frequencies and slope response.

The Fourier spectra of seismic wave acceleration exhibit notable differences before and after passing through the slope. A comparison between the response at the monitoring points A8 and A14 shows that the Fourier spectrum amplitude at A8 is lower than that at A14, highlighting the significant influence of elevation on the Fourier spectrum

amplitude within the slope. It can also be seen that the amplitude exhibits a decreasing trend with increasing elevation. In the dip slope, both A8 and A14 exhibit larger Fourier spectrum amplitudes compared to their counterparts in the anti-dip slope. This observation suggests a greater accumulation of energy at the monitoring points within the dip slope, leading to a stronger dynamic response of the slope. Figs. 8(c) and 8(d) show that the Fourier spectra at the monitoring points A8 and A14 display characteristics of low-frequency absorption relative to the input wave. Under the 0.6 g excitation, the low-frequency absorption rate is 10.9 % at monitoring point A8 and 0.41 % at A14 for the dip slope, while
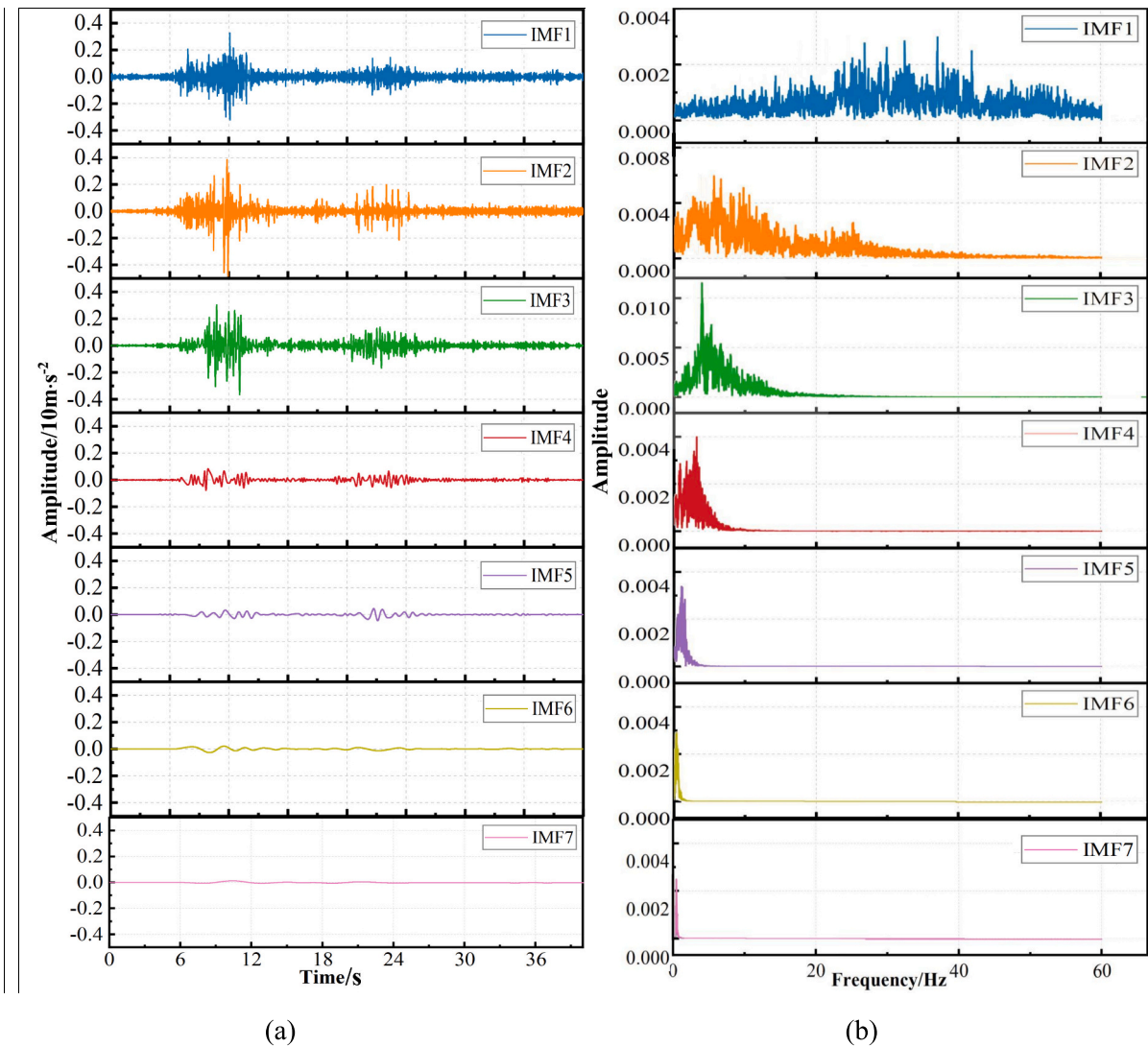
(a)
(b)

Fig. 9. EMD results of acceleration of A8 measuring point under 0.4 g seismic wave: (a) acceleration；(b) instantaneous frequency.

for the anti-dip slope, it is 9.7 % at A8 and 1.5 % at A14. Furthermore, both the slopes exhibit a surge in the amplitude of the Fourier spectrum around 25 Hz, indicating an approximate natural frequency of 25 Hz for the slope. As the seismic wave excitation reaches 0.6 g, the development of numerous cracks affects the integrity of the slope. As discussed before, the seismic wave propagation through the slope results in reflection and refraction, leading to a complex stress field and an amplified amplitude of the high-frequency component. High-frequency component of seismic waves, characterized by shorter periods and higher excitation frequencies, primarily induce local damage in vulnerable slop areas. The rapid excitations associated with high-frequency seismic waves can trigger shear failure or localized fragmentation within the slope.

Fig. 8(e) and Fig. 8(f) present the spectral ratios for the dip slope and anti-dip slope when the peak input acceleration reaches 0.6 g. For the dip slope, in the low-frequency range (0-20 Hz), there is minimal variation in spectral ratios between the top and bottom of the slope. However, in the high-frequency range (frequencies above 20 Hz), there are significant differences in spectral ratios, with the largest difference occurring at 25 Hz. In this series of tests, the dip slope consists of multiple structural planes. When seismic waves propagate through these structural planes, multiple reflections and refractions occur, resulting in wavefield superposition. This effect is particularly pronounced at the top of the slope, where the highest degree of freedom exists. Consequently, higher frequency components are generated near the slope top,

indicating notable terrain effects. Therefore, for the dip slope, the spectral ratio at the top position (A8) was significantly higher than that at the bottom of the slope (A14) in the high-frequency range. Based on transfer function analysis, the natural frequency of the slope is around 25 Hz, which explains the largest difference in spectral ratios at this frequency. Conversely, for the anti-dip slope, there is little variation in spectral ratios between the top and bottom across the entire frequency range. Moreover, the peak spectral ratio of the anti-dip slope is smaller than that of the dip slope, indicating better seismic stability for the anti-dip slope.

4.3. Identifying seismic damage

4.3.1. Hilbert-Huang Transform analysis

In general, seismic waves are characterized by their non-stationary, nonlinear, and time-varying signals, and encompass diverse frequency components that evolve during vibration. Relying solely on the Fourier transform is insufficient for capturing the time characteristics of these frequency components. Therefore, the need for a time-frequency transformation of seismic waves becomes crucial. The Hilbert-Huang Transform (HHT) stands out as an optimal tool for analyzing nonlinear and non-stationary signals due to its adaptive and efficient signal decomposition capabilities (Fan et al., 2019; Li et al., 2023). Hence, in this study the HHT method is employed to analyze the dynamic response
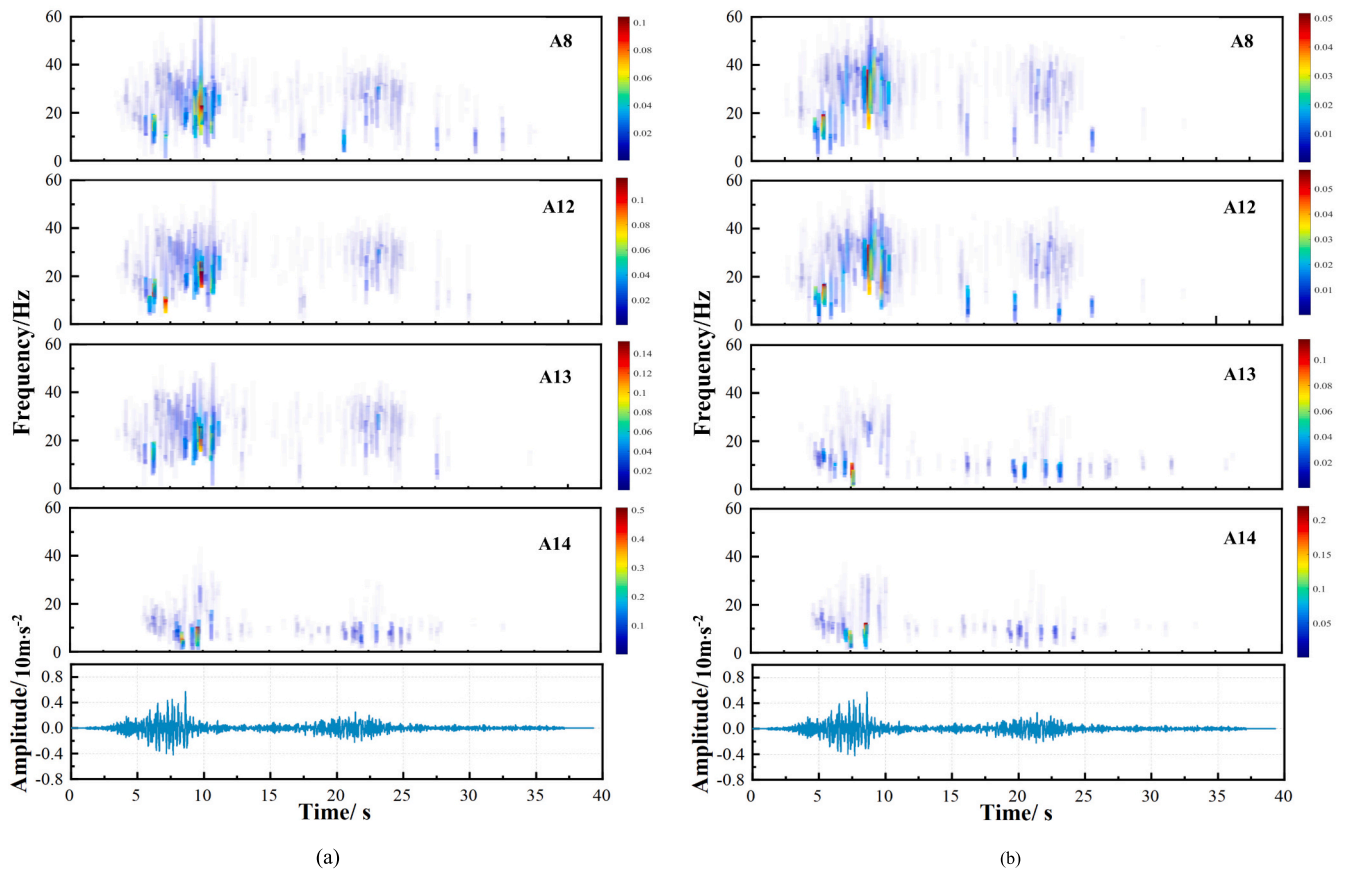
Fig. 10. Hilbert spectrum of dip slope and anti-dip slope models under 0.6 g horizontal Wolong Wave action: (a) Hilbert spectrum of dip slope model at different measuring points; (b) Hilbert spectrum of anti-dip slope model at different measuring points.

characteristics of slopes under seismic actions. Through the HHT method, the relationship between the slope's dynamic response in terms of time, frequency, and amplitude can be obtained (Chen et al., 2022). The analysis of the dynamic response of dip and anti-dip slopes in the time-frequency domain using the HHT method involves two-step process: Empirical Mode Decomposition (EMD) followed by the Hilbert transform. The EMD process begins by treating the seismic signal as a composite signal composed of distinct Intrinsic Mode Functions (IMFs). By applying the Hilbert transform to these IMF components, the instantaneous frequency spectra of each IMF component can be then obtained. The synthesis of the instantaneous frequency spectra from all IMF components yields the distribution characteristics of the seismic signal in the time-frequency domain, represented by the Hilbert spectrum (as shown in Eq. (3)).

$$H(\omega, t) = Re \sum_{i=1}^{n} a_i(t) e^{\int \omega_{i(t)} dt} \qquad (3)$$

where, $a_i(t)$ represents the instantaneous amplitude, $\omega_{i(t)}$ represents the instantaneous frequency, and Re denotes the imaginary part of the real number.

The acceleration time history recorded at the slope shoulder measurement point (A8) of the dip slope, subjected to the WL seismic wave with an amplitude of 0.4 g, was chosen for EMD processing. Fig. 9 presents the extracted 7th order IMF components and their corresponding Fourier spectra. A comparison with the original acceleration time history and its Fourier spectrum reveals that the first four IMF components (IMF1 to IMF4) exhibit more significant amplitudes and encompass a broad spectrum of frequency components. These IMF components replicate the amplitudes and frequencies of the original acceleration time history. Hence, it can be inferred that these first four

IMF components represent the primary components of the original acceleration time history, while the remaining IMF components mainly consist of interference components. This underscores the EMD method's capability in isolating and removing noise from the seismic signal, thereby enhancing the analysis of seismic wave effects on slope stability.

Fig. 10 illustrates the Hilbert spectra at various elevations within the dip and anti-dip slopes under the WL seismic wave with a 0.6 g. The horizontal axis represents the vibration duration, and the vertical axis represents the instantaneous frequency, while the color intensity corresponds to the amplitude at specific moments and frequencies. The figure reveals two distinct concentration areas that correspond to the two prominent exciting periods of the input wave. Specifically, under the WL seismic wave with a 0.6 g, these concentration areas primarily occur within the 5–10 s and 17–23 s intervals. The frequency of the slope predominantly ranges between 10 and 25 Hz, with a notable peak around 25 Hz, indicating the HHT method's capability to depict the propagation characteristics of seismic energy accurately in the time-frequency domain. As the seismic wave propagates from the slope base to its top, the shape and peak values of the Hilbert spectra at different elevations undergo significant changes. The energy concentration areas gradually expand toward higher frequencies with increasing elevation. At the bottom of the slope (A14), the seismic energy's low-frequency component (0–20 Hz) mainly distributes around the 6–8 s, while the high-frequency component (30–50 Hz) is predominantly present around the 8–12 s and 21–23 s intervals. With an increase in elevation, the amplitude of low-frequency energy gradually diminishes, shifting toward the high-frequency range. Notably, at the slope shoulder (A8), seismic energy concentrates between 20 and 50 Hz, featuring multiple peaks at the 7th, 10th, and 11th seconds. This indicates that the slope acts as a filter for low-frequency seismic wave energy, while amplifying the high-frequency component. When
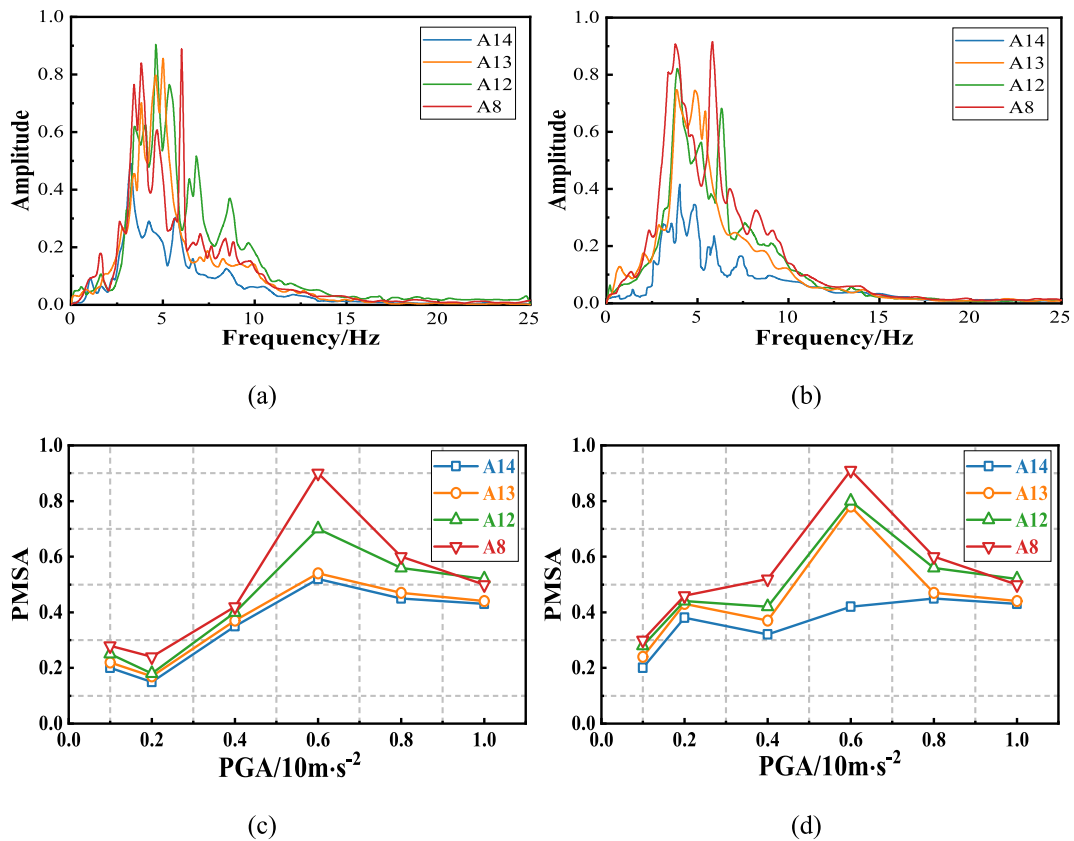
Fig. 11. Marginal spectrum and PMSA of the dip slope model and anti-dip slope model: (a) marginal spectrum of the dip slope model; (b) marginal spectrum of the anti-dip slope model; (c) PMSA variation pattern of dip slope model under different excitation amplitudes; (d) PMSA variation pattern of anti-dip slope model under different excitation amplitudes.

comparing the Hilbert spectra of the dip and anti-dip slopes at various elevations, it becomes evident that the dip slope exhibits greater seismic energy compared to the anti-dip slope.

4.3.2. Marginal SPECTRUM analysis

By performing a time integration of the expression for the Hilbert spectrum, the Hilbert marginal spectrum of the seismic signal can be obtained using the following equation.

$$h(\omega, t) = \int_0^T H(\omega, t)dt \tag{4}$$

The Hilbert marginal spectrum, reflects the global energy distribution of each frequency in the seismic signal (Song et al., 2021a, 2021b, 2021c). Fig. 11 illustrates the marginal spectra of the dip and anti-dip slopes subjected to a 0.6 g seismic wave. From Figs. 11(a) and 11(b) it can be observed that the seismic wave frequency components at different elevations of the slope exhibit significant differences, especially between the upper and lower parts of the slope. As elevation increases (A14-A8), the marginal spectrum's amplitude shows an upward trend. The lower part of the slope concentrates energy in the low-frequency range (3–5 Hz), while the middle and upper parts of the slope exhibit energy concentration within 6–10 Hz. The marginal spectrum at measurement point A14 increases slowly, indicating minimal damage occurred at the slope toe under the 0.6 g seismic wave. With increasing the elevation, the peak amplitude of the marginal spectrum shifts toward higher frequencies. High-frequency components primarily induce localized slope deformation. This change alters the marginal spectrum's shape and the emergence of multiple peaks (e.g., A8), indicating damage at that location. Figs. 11(c) and 11(d) depict the evolution of the peak marginal spectrum amplitude (PMSA) for the dip and anti-dip slopes under different excitation amplitudes, revealing the progressive failure process. Minor changes in PMSA imply slight damage, while sharp changes indicate significant damage. As shown in Fig. 11(c), for the dip slope, slight PMSA reductions under 0.1–0.2 g loading indicate limited seismic energy propagation and minor damage. When the excitation amplitude ranges from 0.4 g to 0.6 g, PMSA starts to increase rapidly, especially in the upper slope (A12 and A8) with growth rates of 75 % and 114 %, respectively. This indicates a more dominant filtering effect on the seismic wave, accelerating cumulative slope failure. Once the excitation amplitude surpasses 0.6 g, PMSA exhibits a decreasing trend at each measurement point, making 0.6 g as a "turning point" for severe slope damage, with A12 and A8 experiencing the most significant amplitude decreases at rates of 25 % and 50 %, respectively. Fig. 11(d) shows that, for the anti-dip slope, as the excitation amplitude ranges from 0.4 g to 0.6 g, PMSA increases rapidly. This results in an accumulating damage that reduces stiffness and increases damping ratio. Once the excitation amplitude exceeds 0.6 g, PMSA at each measurement point displays a decreasing trend. Notably, A13 and A8 exhibit the largest amplitude decreases at rates of 66 % and 52 %, respectively. These results indicate that in the case of dip slope major damage generally occurs at the shoulder (A8), while for the anti-dip slope, significant damage is observed at the second bench (A13) under seismic excitations.

4.4. Comparison of failure modes

During the shaking table tests, high-speed cameras were employed to capture the deformation of the slope models at each stage of seismic loading, facilitating comparative analysis of failure modes between dip and anti-dip rock slopes (Xin et al., 2024b). In general, the shaking table tests revealed a distinct superiority in the stability of the anti-dip slope when compared to the dip slope.
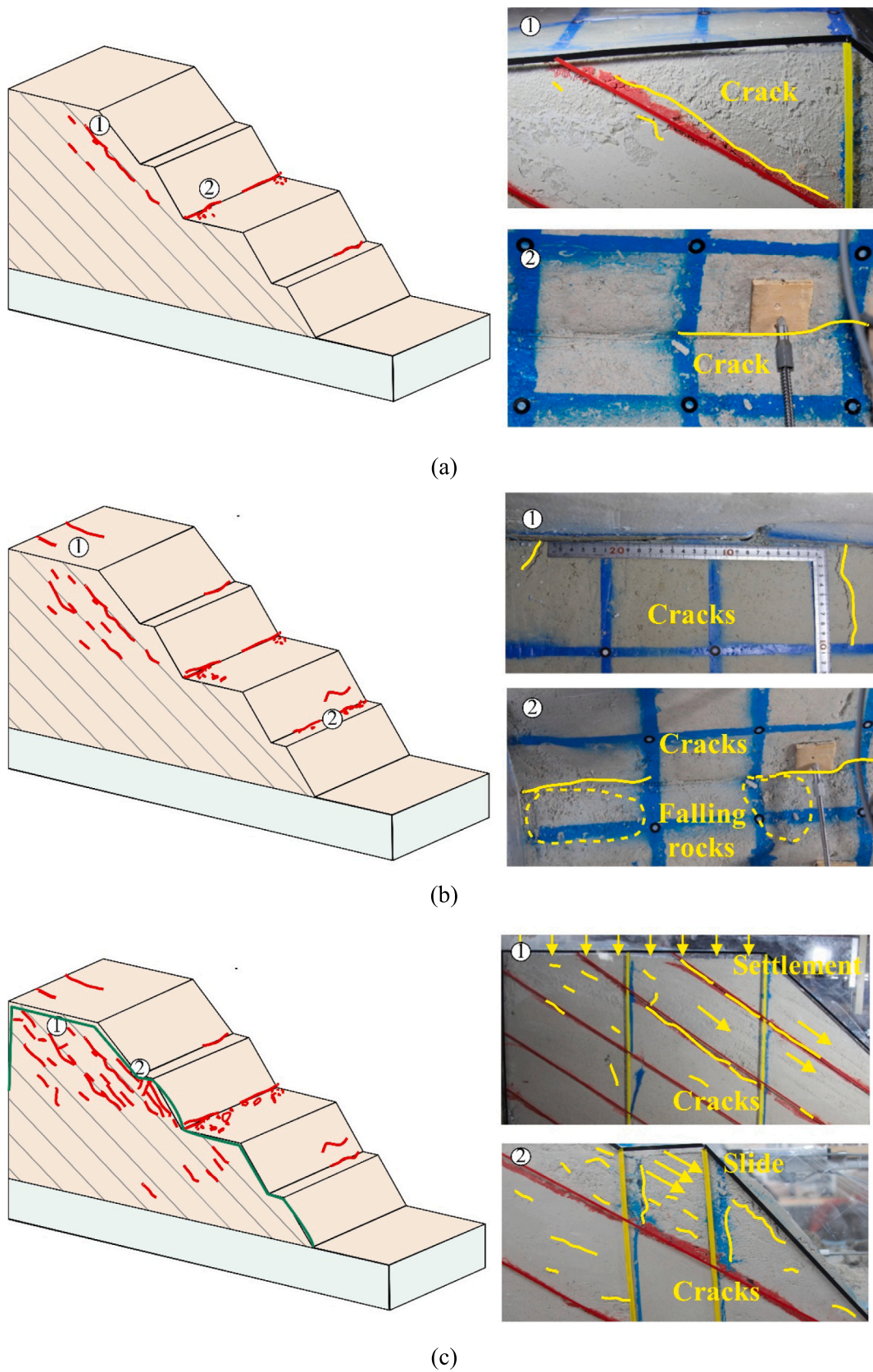
(a)

(b)

(c)

Fig. 12. The failure phenomena of dip model slope subjected to multi-stage seismic excitations: (a) failure phenomena of dip model slope at 0.4 g; (b) failure phenomena of dip model slope at 0.6 g; (c) failure phenomena of dip model slope at 0.8 g; (d) failure phenomena of dip model slope at 1.0 g.
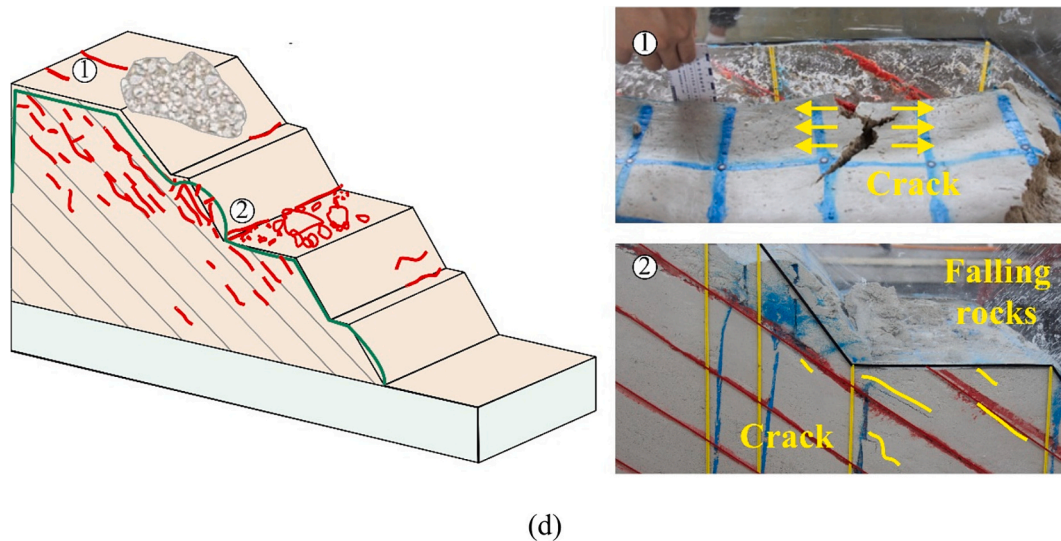
(d)

Fig. 12. (*continued*).

The failure processes of dip and anti-dip slopes are illustrated in Fig. 12 and Fig. 13. For the dip slope, the sequence of failure begins at an excitation amplitude of 0.2 g, where stress concentration and the inertia force of the earthquake initiate tension cracks at the internal corner of the second bench and shear cracks along the structural planes near the slope surface. As the excitation amplitude increased to 0.4 g, the cracks at the internal corner of the second bench widened, causing some rock particles to fall from the slope shoulder. Continuous seismic wave action resulted in cracks appearing at the internal corner of the first bench. When viewed from the slope side, cracks developed along the structural planes near the slope surface. The propagation of seismic waves through the structural planes caused stress concentration and redistribution along the planes, generating tensile stress and the downward extension of cracks along the planes. In rock slopes, cracks typically follow the development of existing joints as they extend downward, leading to increased depth and slope stability deterioration as depicted in Fig. 12 (a). At an excitation amplitude of 0.6 g and under the tensile-shear stress of the seismic waves, cracks at the internal corner of each bench widened, and shear cracks appeared at the slope top (see Fig. 12(b)). At an excitation amplitude of 0.8 g, when viewed from the slope side, cracks that developed along the structural planes alternated between opening and closing due to the tensile-shear action of the seismic waves, and deformation extended into the deeper parts of the slope. The structural planes near the slope surface experienced a maximum separation of 4 mm under the seismic forces, indicating a strong tendency for sliding and detachment along the structural planes away from the slope. The emergence of numerous cracks parallel to the structural planes, increasing in density with elevation, as well as distinct movement toward the free surface of the slope above the boundary of the second bench suggests increased settlement and localized damage in this area. However, the region below this boundary (the first and second benches) remains relatively stable with minimal settlement. This indicates that the wider bench plays a key role in impeding the dynamic response and failure of the slope, limiting potential overall instability to localized damage. The wider platform also facilitates as a catchment for dislodged rock debris from the upper part, and hence contributes to slope stability (as depicted in Fig. 12(c)). When the excitation amplitude reached 1.0 g, the slope shoulder suffered severe damage. At this stage, extensive rock block fell to the second bench while tension cracks were formed at the slope top, indicating dynamic extension with an 8 mm opening displacement. The settlement difference across the second bench boundary was intensified, and the slope toe exhibited bulging (see Fig. 12(d)), indicating advanced stages of failure under high-amplitude seismic activity.

In contrast, the failure process of the anti-dip slope unfolds as follows: Initially, at an excitation amplitude of 0.2 g, no cracks were observed on the slope due to the relatively low seismic energy. When the amplitude increased to 0.4 g, the instantaneous high-energy excitation intensified stress concentration at the internal of the bench, particularly affecting the second wider platform with higher seismic inertia force. This resulted in the initiation of tension cracks at the internal corner of the second bench and the slope toe. These cracks then propagated along the structural planes, and shear cracks parallel to the structural planes appeared on the slope's side as shown in Fig. 13(a). Upon increasing the excitation amplitude to 0.6 g, existing cracks deepened and widened due to the repeated tensile-shear action of the seismic waves. These cracks extended into the slope with a depth of 15 mm and a width of approximately 2 mm along the structural planes. Additionally, a tension crack appeared at the slope top, extending downwards to the internal corner of the third bench as depicted in Fig. 13(b). The slope experienced uneven settlement across different elevations, with larger settlement observed at higher elevations (third bench and slope top) compared to the lower elevations (first bench and second bench). By subsequent increase of the excitation amplitude to 0.8 g, tension cracks appeared at the internal corner of each bench and the slope toe. These cracks propagated downward, segmenting the slope into blocks and fragmenting its internal structure, which significantly compromised its overall integrity. The seismic waves underwent reflection and refraction through multiple crack interfaces, creating a complex stress field, while increasing the filtering effect of the slope (see Fig. 13(c)). When the excitation amplitude reached 1.0 g, the intensified seismic activity further deepened and widened the cracks at the internal corner of the second bench to a depth of 100 mm and a width of 3 mm. Numerous cracks parallel to the shaking direction appeared on the slope, further contributing to significant uneven settlement. The slope top settled by 35 mm, while the second bench settled by 15 mm. Moreover, the rear of the slope continued to experience tension cracking, moving away from the absorbing boundary. The slope toe underwent intense deformation, resulting in noticeable bulging, accompanied by tension cracks at the bulging section as shown in Fig. 13(d).

Fig. 14 presents the final failure phenomena of the dip and anti-dip slopes after experiencing various seismic excitations. A comparative analysis of the failure dynamics under these conditions shows a variance in the onset acceleration for dynamic deformation between the slopes. Specifically, the results indicate that tensile cracks occur at the internal corner of second bench and shear cracks along the structural plane in the
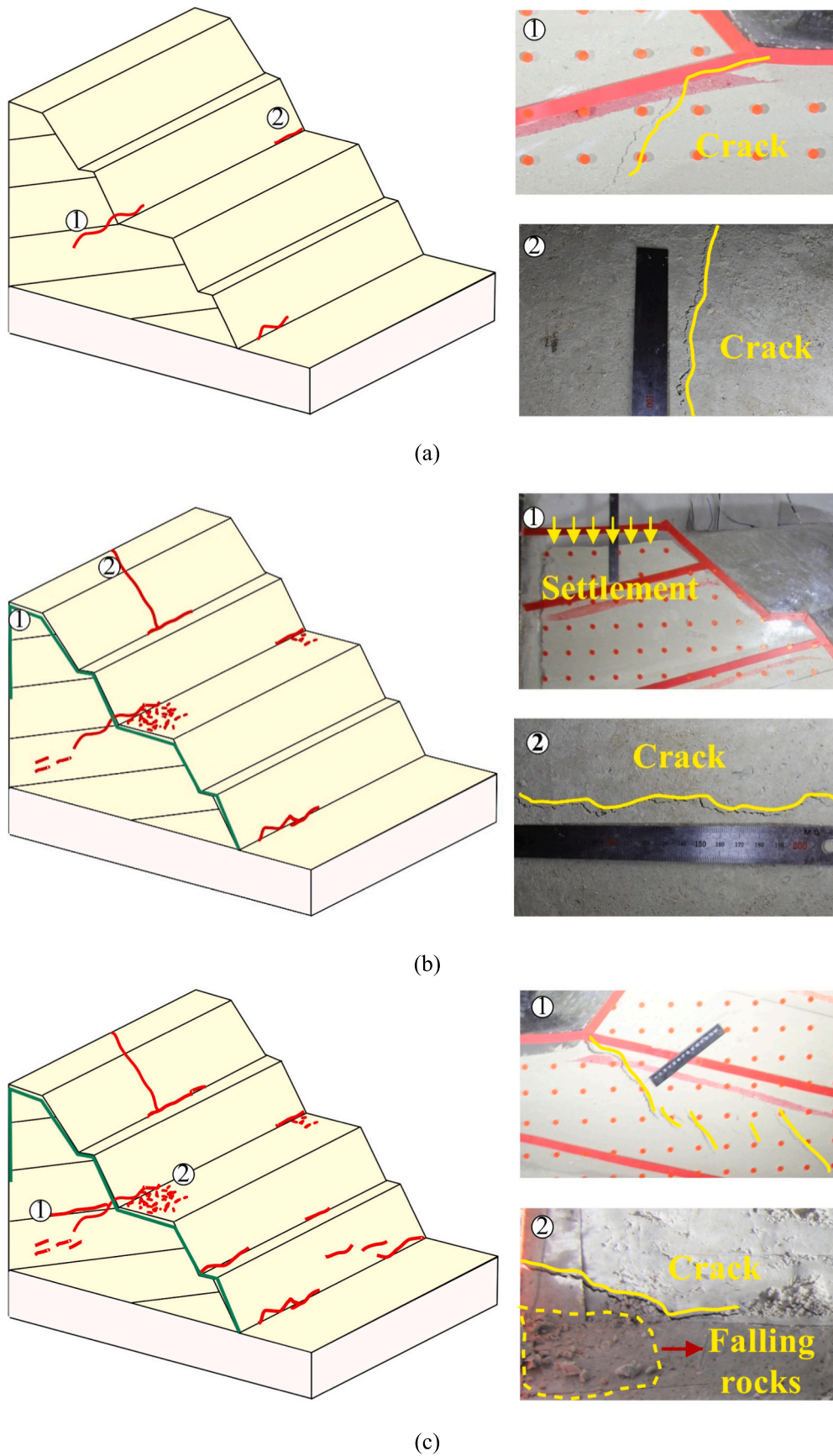
(a)

(b)

(c)

Fig. 13. The failure phenomena of anti-dip slope model subjected to multi-stage seismic excitations: (a) failure phenomena of anti-dip slope at 0.4 g; (b) failure phenomena of anti-dip slope at 0.6 g; (c) failure phenomena of anti-dip slope at 0.8 g; (d) failure phenomena of anti-dip slope at 1.0 g.
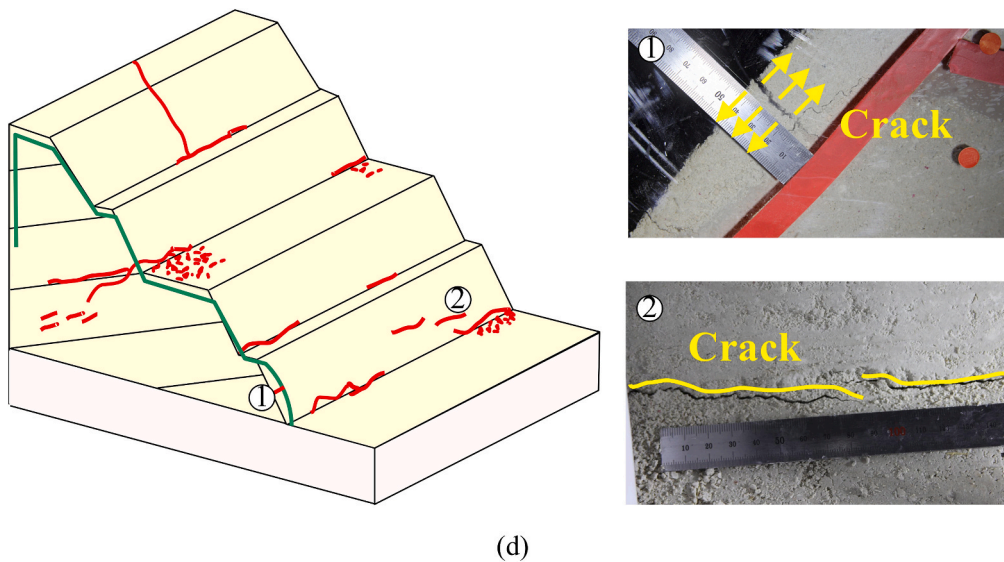
(d)

Fig. 13. (*continued*).

dip slope model at an excitation amplitude of 0.2 g. Conversely, the anti-dip slope model demonstrates tensile cracks at the internal corner of second bench and slope toe at an excitation amplitude of 0.4 g. Moreover, distinct dynamic failure modes are exhibited by the dip and anti-dip slope models. The dynamic failure of the dip slope is primarily categorized as tensile sliding along the structural plane, leading to rockfall at the slope shoulder and fragmentation at the slope top. Conversely, the dynamic failure mode of the anti-dip slope mainly presents as cracks along the internal corner of the second bench, extending downward along the structural plane, and bulging at the front edge of the slope toe.

The observed failure characteristics at each loading increment allow for the categorization of the slope failure process into distinct stages (Liu et al., 2021; Zang et al., 2022). For the dip slope, the failure process encompasses the following stages: elastic failure stage (0.1–0.2 g), plastic failure stage (0.2–0.6 g), cumulative failure stage (0.6–0.8 g), and shear sliding failure stage (0.8–1.0 g). On the other hand, the failure process of the anti-dip slope comprises the elastic failure stage (0.1–0.4 g), plastic failure stage (0.4–0.6 g), cumulative failure stage (0.6–0.8 g), and instability failure stage (0.8–1.0 g).

5. Discussion

5.1. Structural plane angle influence factor

To quantify the differences in dynamic responses between the dip and anti-dip slopes, a dimensionless coefficient called "structural plane angle influence coefficient" (R_a) is introduced. R_a is defined as the ratio of the AAF at the same monitoring point in the dip slope model to that in the anti-dip slope model as shown in the following equation:

$$R_\mathrm{a} = \frac{AAF_b}{AAF_a} \tag{5}$$

where, AAF_b represents the AAF of the dip slope, and AAF_a is the AAF of the anti-dip slope.

Fig. 15 illustrates the impact of variations in the structural plane angle on the acceleration response in the dip and anti-dip slope models. Upon comparing Figs. 15(a) and 15(b), it is observed that when the excitation amplitude reaches 0.4 g, the acceleration response at monitoring point A8 in the dip slope is lower than that in the anti-dip slope ($R_a < 1.0$). This finding suggests that the dip slope has already experienced failure at the slope shoulder at 0.4 g, leading to reduced slope

integrity and an enhanced the filtering effect. At the monitoring point A6, positioned at the external corner of the third bench, the dynamic response difference between the dip and anti-dip slopes becomes more pronounced with increasing excitation amplitude, peaking at 1.0 g with $R_a = 1.11$. Conversely, at the same elevation within the slope, specifically monitoring point A12, the distinction in dynamic response between the dip and anti-dip slopes remains minimal during small amplitude excitations (0.2–0.4 g). However, once the excitation amplitude reaches 0.6 g, the difference in dynamic response between the dip and anti-dip slopes reaches its maximum with $R_a = 1.05$, and as excitation amplitude increases further, this difference gradually decreases. This pattern indicates that at the earthquake intensity level of 0.6 g, the dip slope has developed numerous cracks, especially where relative elevation h/H > 0.5, absorbing high seismic energy and diminishing dynamic response in the affected areas. Therefore, 0.6 g represents the critical excitation amplitude for severe slope failure. At the monitoring point A4, positioned at the second bench, and the monitoring point A13, situated at the same elevation, the difference in dynamic response between the dip and anti-dip slopes gradually decreases as the excitation amplitude increases. Regarding the monitoring point A2, located at the first bench, minimal differences in dynamic response between the dip and anti-dip slopes are observed during small amplitude excitations (0.2–0.4 g). Once the excitation amplitude reaches 0.6 g, both slopes exhibit maximum dynamic response with $R_a = 1.08$. Subsequently, as the excitation amplitude continues to increase, the difference in dynamic response between the dip and anti-dip slopes gradually diminishes. At the monitoring point A14, a peak Ra value of 1.07 is observed at 0.6 g excitation. This suggests that when h/H < 0.5 and during lower amplitude excitations (0.2–0.4 g), the influence of the structural plane angle on the slope's dynamic response is relatively minor. However, as the excitation amplitude reaches 0.6 g, the tendency for sliding along the structural plane becomes apparent in the dip slope, and the distinction in dynamic response between the dip and anti-dip slopes becomes more pronounced.

5.2. Arias intensity

This section aims is to obtain a critical excitation amplitude that can effectively capture the variation process of the slope's dynamic response. This is achieved by integrating the acceleration, Arias intensity, and the dynamic characteristics of the model slopes during the excitation process. Arias intensity, initially proposed by Arias in 1970, is calculated by integrating the squared acceleration values recorded by a
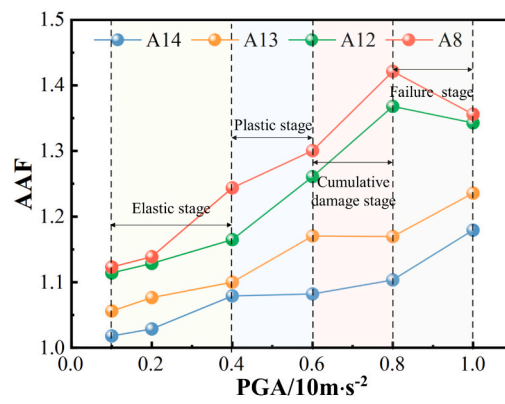
(a)
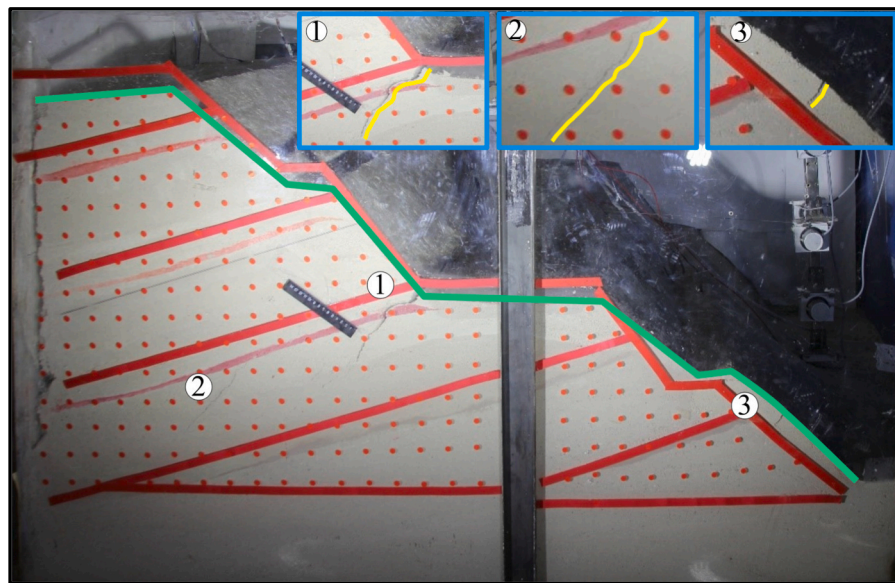
(b)
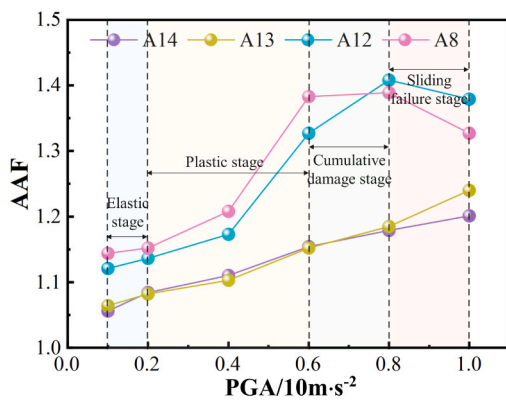
(c)

(d)

Fig. 14. The final failure phenomena and failure process of dip and anti-dip slopes: (a) the final failure phenomena of dip slope; (b) the final failure phenomena of anti-dip slope; (c) the failure process of dip slope; (d) the failure process of anti-dip slope.
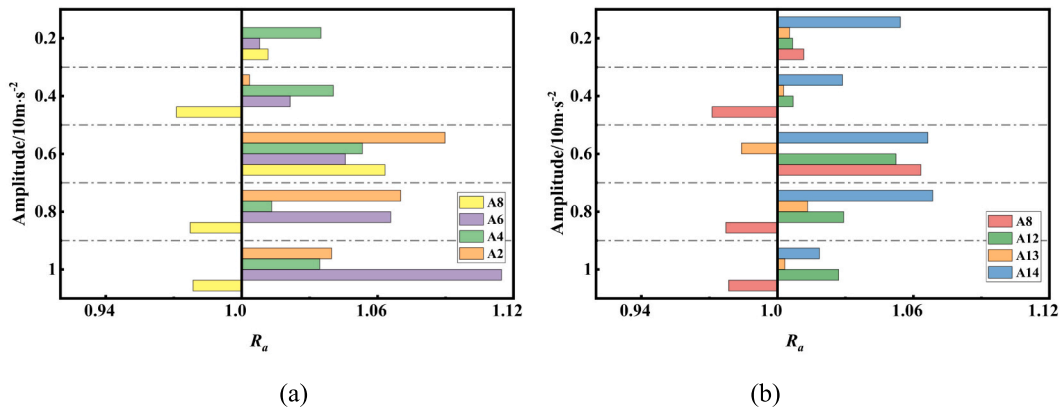
Fig. 15. The R_a for the slope surface and the inside of slope body at different excitation amplitudes: (a) The R_a for the slope surface at different excitation amplitudes; (b) The R_a for the inside of slope body at different excitation amplitudes.
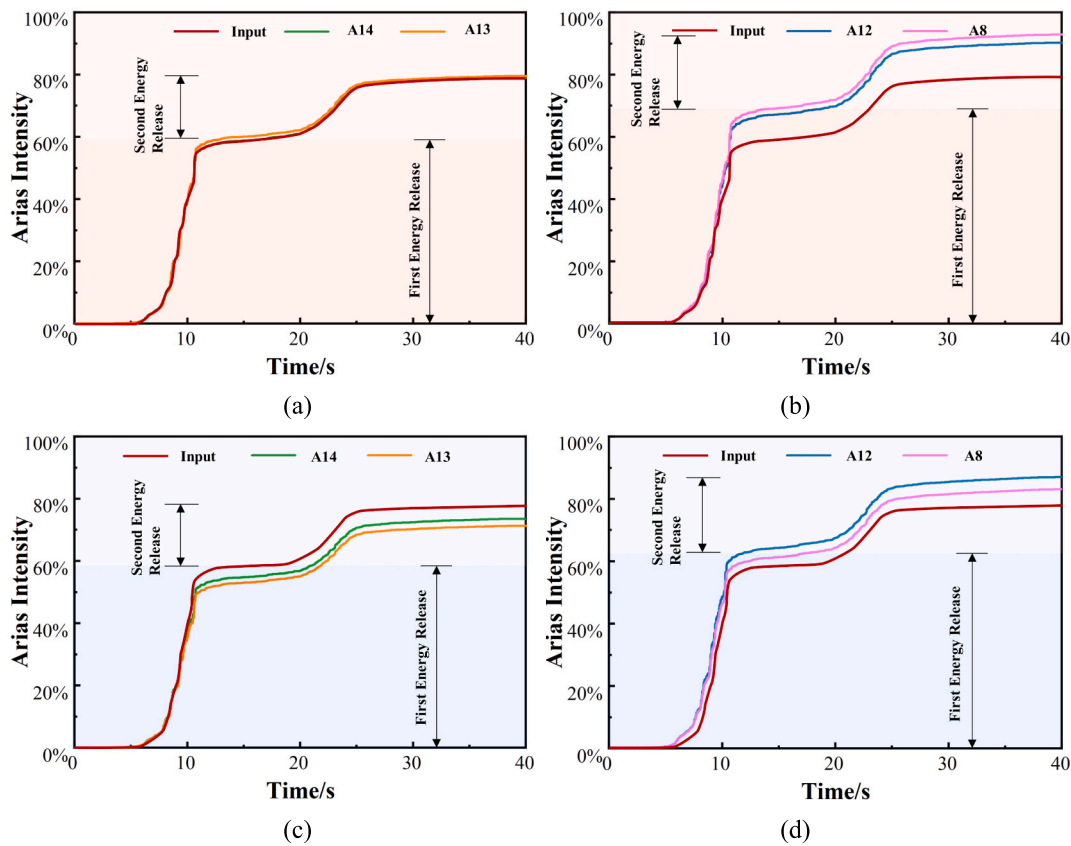

Fig. 16. Time-history curves of Arias intensity for dip and anti-dip slopes: (a) Arias intensity at monitoring points A14 and A13 in the dip slope; (b) Arias intensity at monitoring points A12 and A8 in the dip slope; (c) Arias intensity at monitoring points A14 and A13 in the anti-dip slope; (d) Arias intensity at monitoring points A12 and A8 in the anti-dip slope.

strong motion seismograph over the duration of vibration (Bradley, 2015). Unlike peak acceleration, Arias intensity considers additional factors such as seismic motion amplitude, duration, and frequency, offering a more comprehensive representation of the seismic energy released at the recording site, as shown in Eq. (6).

$$I_a = \frac{\pi}{2g} \int_0^{T_d} [a(t)]^2 dt \qquad (6)$$

where, I_a represents the Arias intensity; and T_d is the duration recorded by the strong motion seismograph.

Fig. 16 depicts the variation of Arias intensity over time for the dip and anti-dip slopes under an excitation amplitude of 0.6 g, reflecting the energy release process of the seismic waves on the slopes. A clear trend of increasing Arias intensity with elevation is observed from monitoring points A14-A8 on both slopes. This trend is a direct result of the positive correlation between Arias intensity and acceleration in the time domain, signifying an elevation amplification effect (EAE). The seismic waves exhibit an initial energy release concentrated within the time range of 5–10 s, followed by a secondary energy release occurring between 17 and 23 s and aligned with the timing of the two energy releases in the acceleration time history. As shown in Fig. 16(b), the initial energy release rate at the monitoring point A8 on the dip slope reaches 70 %, while the subsequent energy release rate is 23 %. Fig. 16(d) shows that
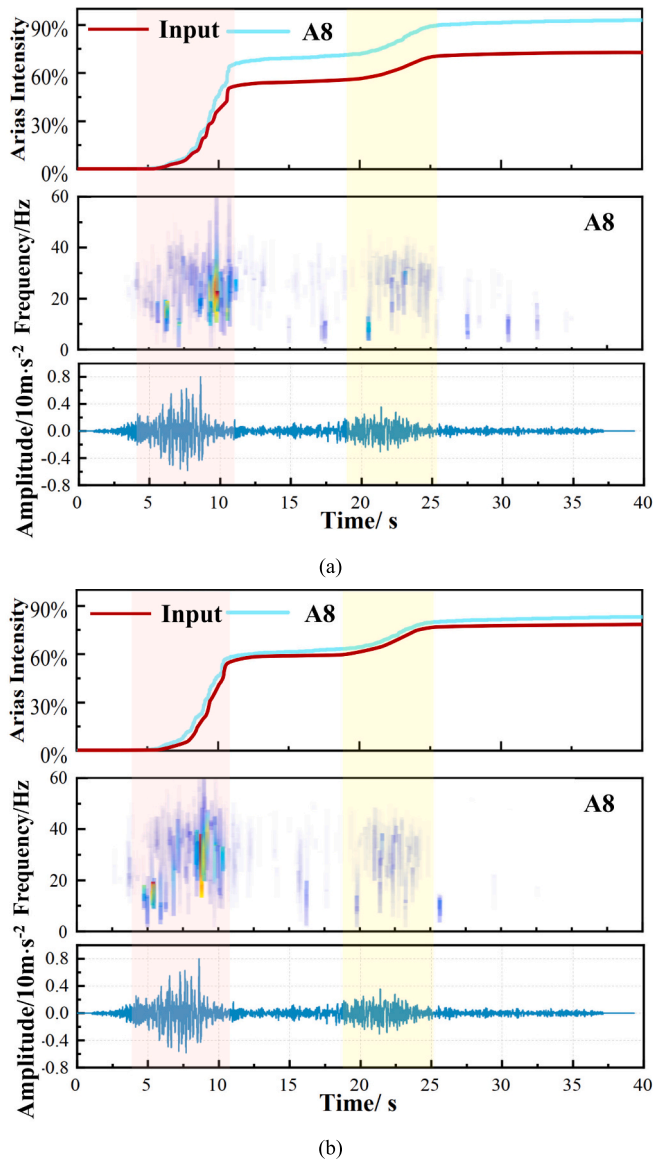
Fig. 17. Hilbert spectrum and Arias intensity at monitoring point A8 during horizontal Wolong wave loading in dip and anti-dip slopes: (a) Hilbert spectrum and Arias intensity at monitoring point A8 during horizontal Wolong wave loading in dip slope; (b) Hilbert spectrum and Arias intensity at monitoring point A8 during horizontal Wolong wave loading in anti-dip slope.

at the same monitoring point on the anti-dip slope, the initial energy release rate is 62 %, with the secondary energy release rate equal to 20 %. The dip slope in this case exhibits a higher energy release rate than the anti-dip slope, which can be attributed to their distinct propagation and reflection behavior of seismic waves. As seismic waves propagate into the dip slope, they encounter less damping and scattering due to the alignment of geological layers with the slope inclination direction. This propagation characteristic fosters energy accumulation within the dip slope and facilitates more effective energy release into the slope body, contributing to an elevated energy release rate. Conversely, the anti-dip slope features geological layers opposing the slope inclination, leading to more damping and scattering during wave propagation, resulting in a lower energy release rate compared to the dip slope. Notably, the initial energy release rate of the Wolong seismic wave significantly surpasses the secondary energy release rate, indicating that slope failure is primarily triggered by the initial strong energy release of the Wolong wave.

Fig. 17 presents a synthesis of acceleration, Hilbert-Huang Transform (HHT), and Arias intensity parameters for both dip and anti-dip slopes,

enabling a comprehensive analysis of their seismic response in the time domain. Acceleration serves as direct observation data for seismic motion, while HHT analysis shows the influence of different frequency components on the slope, and Arias intensity is used as an indicator of seismic motion intensity. The time history of Arias intensity is segmented into distinct stages, including the initial stage, the mainshock stage, and the aftershock stage, each representing different stages of seismic wave energy release. By synthesizing the analysis of these three parameters, a more thorough evaluation of the slope's seismic response characteristics can be achieved, which provides valuable insights for slope engineering design and seismic hazard risk management.

6. Conclusion

This study aimed to investigate the dynamic response of both dip and anti-dip rock slopes, through seismic simulations on a shaking table, with incremental loading using the Wolong wave. The conducted analysis covered time domain characteristics of the acceleration, frequency domain characteristics, and time-frequency characteristics. Additionally, by integrating the analysis of acceleration, Arias intensity, and the dynamic characteristics of the model slopes during the excitation process, the critical excitation amplitude for each case was determined. The key findings of this study are summarized as follows:

(1) Under the action of 0.6 g WL wave, notable differences in the Hilbert spectra between dip and anti-dip slopes were observed. With increasing elevation, the energy concentration area expanded progressively toward higher frequencies. The seismic wave energy amplitude was greater in the dip slope compared to the anti-dip slope, however, differences in their time and frequency domain distributions remained minimal.

(2) Significant differences in marginal spectra were observed between the dip and anti-dip slopes when subjected to the 0.6 g WL wave. During the 0.4–0.6 g loading, the dip slope exhibited accelerated failure, with the most severe damage occurring at the upper parts. Similarly, the anti-dip slope showed increased damage within the same loading range, particularly at the second bench. The 0.6 g threshold represented a "turning point" for substantial slope failure, characterized by significant damage to the shoulder of the dip slope and severe damage to the second bench of the anti-dip slope.

(3) The introduction of the dimensionless coefficient "structural plane angle influence coefficient" R_a enabled a quantitative characterization of the dynamic response differences between the dip and anti-dip slopes. At relative elevations h/H < 0.5 and lower excitation amplitudes (0.2–0.4 g), the impact of the structural plane angle on the slope's dynamic response was relatively insignificant. However, upon reaching 0.6 g excitation amplitude, sliding tendencies along the structural plane in the dip slope becomes more evident, underscoring distinct dynamic response differences between the slope types. This observation firmly establishes the 0.6 g excitation amplitude as the critical threshold beyond which severe damage to slopes is likely to occur.

(4) The Arias intensity of the slopes demonstrated an elevation-dependent amplification effect, with the dip slope exhibiting a higher rate of energy release compared to the anti-dip slope. This suggests that the dip slope is more susceptible to seismic motion, characterized by enhanced energy accumulation and release, thereby escalating the potential for slope failure.

It should be noted that the findings presented in this study are specific to the conditions of the slopes examined here. Nevertheless, the general conclusions are expected to be applicable to various types of dip and anti-dip rock slopes. These insights should prove useful for more efficient design and assessment of such systems. By understanding the

critical excitation thresholds and dynamic responses, engineers and geologists can better predict and mitigate potential slope failures, enhancing the safety and stability of rock slopes in seismic regions.

CRediT authorship contribution statement

Chunlei Xin: Writing – review & editing, Supervision, Resources, Project administration, Investigation, Funding acquisition, Conceptualization. **Wenhui Li:** Writing – original draft, Formal analysis, Data curation. **Zhao Wang:** Writing – review & editing, Validation, Supervision, Project administration, Methodology, Formal analysis, Conceptualization. **Wenkai Feng:** Investigation, Resources. **Iman Hajirasouliha:** Writing – review & editing. **Xinyuan Yu:** Writing – review & editing, Visualization.

Declaration of competing interest

The authors declare that they have no known competing financial interests or personal relationships that could have appeared to influence the work reported in this paper.

Data availability

Data will be made available on request.

Acknowledgements

References

Bao, Y.J., Huang, Y., Zhu, C.Q., 2021. Effects of near-fault ground motions on dynamic response of slopes based on shaking table model tests. Soil Dyn. Earthq. Eng. 149.

Bradley, B.A., 2015. Correlation of Arias intensity with amplitude, duration and cumulative intensity measures. Soil Dyn. Earthq. Eng. 78, 89–98.

Che, A.L., Yang, H.K., Wang, B., Ge, X.R., 2016. Wave propagations through jointed rock masses and their effects on the stability of slopes. Eng. Geol. 201, 45–56.

Chen, C.C., Li, H.H., Chiu, Y.C., Tsai, Y.K., 2020. Dynamic response of a physical anti-dip rock slope model revealed by shaking table tests. Eng. Geol. 277, 105772.

Chen, J.C., Wang, L.M., Wang, P., Che, A.L., 2022. Failure mechanism investigation on loess-mudstone landslides based on the Hilbert-Huang transform method using a large-scale shaking table test. Eng. Geol. 302, 106630.

Chen, J.C., Che, A.L., Wang, L.M., 2023. Cumulative damage evolution rule of rock slope based on shaking table test using VMD-HT. Eng. Geol. 314, 107003.

Cui, S.H., Pei, X.J., Yang, H.L., Zhu, L., Jiang, Y., Zhu, C., Jiang, T., Huang, R.Q., 2023. Bedding slope damage accumulation induced by multiple earthquakes. Soil Dyn. Earthq. Eng. 173.

Cui, S.H., Pei, X.J., Huang, R.Q., Zhu, L., Yang, H.L., Liang, Y.F., Zhu, C., 2024. The analysis of seismic induced progressive instability and failure mechanisms: a case study. Int. J. Rock Mech. Min. Sci. 174.

Dong, J.Y., Wang, C., Huang, Z.Q., Yang, J.H., Xue, L., 2022. Shaking Table Model Test to Determine Dynamic Response Characteristics and failure Modes of Steep Bedding Rock Slope. Rock Mech. Rock. Eng. 55 (6), 3645–3658.

Fan, G., Zhang, J.J., Wu, J.B., Yan, K.M., 2016. Dynamic Response and Dynamic failure Mode of a Weak Intercalated Rock Slope using a Shaking Table. Rock Mech. Rock. Eng. 49 (8), 3243–3256.

Fan, G., Zhang, L.M., Zhang, J.J., Yang, C.W., 2019. Analysis of Seismic Stability of an Obsequent Rock Slope using Time-Frequency Method. Rock Mech. Rock. Eng. 52 (10), 3809–3823.

He, J.X., Qi, S.W., Wang, Y.S., Saroglou, C., 2020. Seismic response of the Lengzhuguan slope caused by topographic and geological effects. Eng. Geol. 265.

Hu, W., Xin, C.L., Li, Y., Zheng, Y.S., van Asch, T.W.J., McSaveney, M., 2021. Instrumented flume tests on the failure and fluidization of tailings dams induced by rainfall infiltration. Eng. Geol. 294, 106401.

Hu, X.L., Liu, D.Z., Zheng, W.B., Tannant, D., Kang, C., 2024. 1-g physical modeling in engineering geology and its application of pile-reinforced reservoir landslides. Eng. Geol. 331, 107450.

Li, L.Q., Ju, N.P., Sheng, D.C., 2023. Seismic performance and failure mechanism of interbedded slopes with steep rock layers. Eng. Geol. 326, 107312.

Liu, H.D., Zhao, Y.W., Dong, J.Y., Wang, Z.F., 2021. Experimental study of the dynamic response and failure mode of anti-dip rock slopes. Bull. Eng. Geol. Environ. 80 (8), 6583–6596.

Ning, Y.B., Zhang, G.C., Tang, H.M., Shen, W.C., Shen, P.W., 2019. Process analysis of toppling failure on anti-dip rock slopes under seismic load in Southwest China. Rock Mech. Rock. Eng. 52 (11), 4439–4455.

Qi, S.W., He, J.X., Zhan, Z.F., 2022. A single surface slope effects on seismic response based on shaking table test and numerical simulation. Eng. Geol. 306, 106762.

Song, D.Q., Che, A.L., Zhu, R.J., Ge, X.R., 2019. Natural Frequency Characteristics of Rock Masses Containing a complex Geological Structure and their Effects on the Dynamic Stability of Slopes. Rock Mech. Rock. Eng. 52 (11), 4457–4473.

Song, D.Q., Liu, X.L., Huang, J., Zhang, J.M., 2021a. Energy-based analysis of seismic failure mechanism of a rock slope with discontinuities using Hilbert-Huang transform and marginal spectrum in the time-frequency domain. Landslides 18 (1), 105–123.

Song, D.Q., Liu, X.L., Huang, J., Zhang, Y.F., Zhang, J.M., Nkwenti, B.N., 2021b. Seismic cumulative failure effects on a reservoir bank slope with a complex geological structure considering plastic deformation characteristics using shaking table tests. Eng. Geol. 286, 106085.

Song, D.Q., Liu, X.L., Li, B., Zhang, J.M., Bastos, J.J.V., 2021c. Assessing the influence of a rapid water drawdown on the seismic response characteristics of a reservoir rock slope using time–frequency analysis. Acta Geotech. 16 (4), 1281–1302.

Tai, D.P., Qi, S.W., Zheng, B.W., Luo, G.M., He, J.X., Guo, S.F., Zou, Y., Wang, Z., 2024. Effect of excitation frequency and joint density on the dynamic amplification effect of slope surface on jointed rock slopes. Eng. Geol. 330, 107385.

Wen, Y.M., Xin, C.L., Shen, Y.S., Huang, Z.M., Gao, B., 2021. The seismic response mechanisms of segmental lining structures applied in fault-crossing mountain tunnel: the numerical investigation and experimental validation. Soil Dyn. Earthq. Eng. 151, 107001.

Xin, C.L., Wang, Z.Z., Gao, B., 2018. Shaking table tests on seismic response and damage mode of tunnel linings in diverse tunnel-void interaction states. Tunn. Undergr. Space Technol. 77, 295–304.

Xin, C.L., Wang, Z.Z., Zhou, J.M., Gao, B., 2019. Shaking table tests on seismic behavior of polypropylene fiber reinforced concrete tunnel lining. Tunn. Undergr. Space Technol. 88, 1–15.

Xin, C.L., Wang, Z.Z., Yu, J., 2020. The evaluation on shock absorption performance of buffer layer around the cross section of tunnel lining. Soil Dyn. Earthq. Eng. 131, 106032.

Xin, C.L., Wang, Z., Hajirasouliha, I., Yang, F., Li, W.H., Chen, T., Gao, B., 2022. Seismic response mechanisms of casing-shape composite tunnel lining: Theoretical analysis and shaking table test verification. Soil Dyn. Earthq. Eng. 162, 107440.

Xin, C.L., Shuai, Y.X., Song, D.Q., Liu, X.L. 2024a. Dynamic interaction and failure mechanism in tunnel-slope systems: Mitigation insights from shaking table tests and numerical analysis. Tunnelling and Underground Space Technology. 152. 105940.

Xin, C.L., Yang, F., Feng, W.K., Wang, Z., Li, W.H., 2024b. Seismic responses and shattering cumulative effects of bedding parallel stepped rock slope: Model test and numerical simulation. J. Rock Mech. Geotech. Eng. 1614, 31. https://doi.org/10.1016/j.jrmge.2024.03.031.

Xu, X., Huang, Y., Yashima, A., Du, X.L., 2022. Failure evolution process of pile-anchor reinforced rock slope based on centrifuge shaking table tests. Eng. Geol. 311, 106920.

Xu, M., Yu, X.Y., Pan, Y.H., Liu, X.S., Zhao, Y.P., Hu, J.J., 2023. Analysis of the seismic dynamic response and failure mode of the Layue landslide. Landslides 20 (6), 1135–1148.

Yang, G.X., Qi, S.W., Wu, F.Q., Zhan, Z.F., 2018. Seismic amplification of the anti-dip rock slope and deformation characteristics: a large-scale shaking table test. Soil Dyn. Earthq. Eng. 115, 907–916.

Yang, H.L., Cui, S.H., Pei, X.J., Fan, X.M., Lei, J., 2023a. Multiple earthquake-induced progressive failure of bedding slopes with a saturated weak layer: Shaking table model tests. Soil Dyn. Earthq. Eng. 170, 107906.

Yang, C.W., Tong, X.H., Chen, G.P., Yuan, C., Lian, J., 2023b. Assessment of seismic landslide susceptibility of bedrock and overburden layer slope based on shaking table tests. Eng. Geol. 323, 107197.

Zang, M.D., Yang, G.X., Dong, J.Y., Qi, S.W., He, J.X., Liang, N., 2022. Experimental study on seismic response and progressive failure characteristics of bedding rock slopes. J. Rock Mech. Geotech. Eng. 14 (5), 1394–1405.

Zhao, L.Y., Huang, Y., Hu, H.Q., 2020. Stochastic seismic response of a slope based on large-scale shaking-table tests. Eng. Geol. 277, 105782.